2020-06-11

Threedimensional structure, ground rupture hazards, and static stress models for complex nonplanar thrust faults in the Ventura basin, southern California

Hughes, A

10.1029/2020jb019539
Journal of Geophysical Research: Solid Earth
American Geophysical Union (AGU)

Hughes Alex (Orcid ID: 0000-0002-4866-1006)
Mildon Zoe, K (Orcid ID: 0000-0001-6192-765X)
Rood Dylan, H (Orcid ID: 0000-0002-4425-4702)
Rockwell Thomas, K. (Orcid ID: 0000-0001-5319-6447)
Marshall Scott, T. (Orcid ID: 0000-0001-8879-6514)

Three-dimensional structure, ground rupture hazards, and static stress models for complex non-planar thrust faults in the Ventura basin, southern California

A. Hughes[1,2], R. E. Bell[1], Z. K. Mildon[4], D. H. Rood[1,3], A. C. Whittaker[1], T. K. Rockwell[5], Y. Levy[5,9], D. E. DeVecchio[6], S. T. Marshall[7], C. Nicholson[8]

[1] Department of Earth Science and Engineering, Imperial College, London, U.K.

[2] Institut de Physique du Globe de Paris (CNRS UMR7154), Paris, France

[3] Earth Research Institute, University of California, Santa Barbara, California, USA

[4] School of Geography, Earth and Environmental Sciences, University of Plymouth, Plymouth, U.K.

[5] San Diego State University, San Diego, California, USA

[6] School of Earth and Space Exploration, Arizona State University, Phoenix, Arizona, USA

[7] Department of Geological and Environmental Sciences, Appalachian State University, Boone, North Carolina, USA

[8] Marine Science Institute, University of California, Santa Barbara, USA

[9] Scripps Institution of Oceanography, University of California, San Diego, La Jolla, California, USA

Corresponding author: Alex Hughes (hughes@ipgp.fr)

Key Points

Three-dimensional geometry of the low-angle SSCF, a significant ground rupture hazard, quantified by drilling data

This article has been accepted for publication and undergone full peer review but has not been through the copyediting, typesetting, pagination and proofreading process which may lead to differences between this version and the Version of Record. Please cite this article as doi: 10.1029/2020JB019539

Simple method presented for creating complex geometry faults as inputs for models of static Coulomb stress change

Earthquakes on the Ventura and Pitas Point faults may influence the location and magnitude of seismicity on the San Cayetano fault

Key words (x 6)

Southern San Cayetano fault, Ventura Basin, seismic hazard, static Coulomb stress transfer, thrust faults, multi-fault ruptures

Abstract

To investigate the subsurface geometry of a recently discovered, seismically-active fault in the Ventura basin, southern California, USA, we present a series of cross sections and a new three-dimensional fault model across the Southern San Cayetano fault (SSCF) based on integration of surface data with petroleum industry well-log data. Additionally, the fault model for the SSCF, along with models of other regional faults extracted from the Southern California Earthquake Center three-dimensional Community Fault Model, are incorporated in static Coulomb stress modeling to investigate static Coulomb stress transfer between thrust faults with complex geometry and to further our understanding of stress transfer in the Ventura basin. The results of the subsurface well investigation provide evidence for a low-angle SSCF that dips ~15° north and connects with the western section of the San Cayetano fault around 1.5–3.5 km depth. We interpret the results of static Coulomb stress models to partly explain contrasting geomorphic expression between different sections of the San Cayetano fault and a potential mismatch in timings between large-magnitude uplift events suggested by paleoseismic studies on the Pitas Point, Ventura, and San Cayetano faults. In addition to new insights into the structure and potential rupture hazard of a recently discovered active reverse fault in a highly populated area of southern California, this study provides a simple method to model static Coulomb stress transfer on complex geometry faults in fold and thrust belts.

1. Introduction

Characterizing the three-dimensional geometry of faults in the subsurface is crucial to investigate how structural complexities in fault geometry can affect models of static stress distribution and rupture propagation (Oglesby et al., 1998; Oglesby and Day, 2001; Ryan et al., 2015; Mildon et al., 2016; Biasi and Wesnousky, 2017; Douilly et al., 2020). Moreover, the importance of having an accurate understanding of the three-dimensional fault network geometry to improve assessment of seismic hazard has been brought into focus by several recent large-magnitude earthquakes that propagated along multiple faults with complex geometry and kinematics. For example, the 2016 M_w 7.8 Kaikōura earthquake, New Zealand (Hamling et al., 2017), the 2010 M_w 7.2 El Mayor-Cucapah earthquake, Mexico (Fletcher et al., 2014; Fletcher et al., 2016), and the 2010 M_w 7.1 Darfield earthquake, New Zealand (Beavan et al., 2012; Quigley et al., 2019) all involved slip on multiple faults with various orientations and senses of slip. During the Kaikōura earthquake, small faults that may have been previously interpreted to represent low seismic hazard played a key role in enhancing both fault connectivity and stress transfer during the event (Clark et al., 2017; Hamling et al., 2017). However, despite potentially playing an important role in enhancing stress transfer, small offset and/or young faults can sometimes be overlooked because they may not have pronounced stratigraphic offset and are difficult to identify in subsurface data (Hughes et al., 2018; Pei et al., 2018).

Although it is well-known that faults are non-planar (e.g., Plesch et al., 2007; Candela et al., 2011; Nicholson et al., 2017a), studies that model static Coulomb stress transfer have routinely employed simplified planar fault geometries (e.g., Harris and Simpson, 1992; Lin and Stein, 2004; Pace et al., 2014; Mohammadi et al., 2019). Recent work has attempted to address this issue and studies indicate that fault geometry exerts a strong control on the magnitude of stress transfer between faults by altering patterns of local stress distribution (Marshall and Morris, 2012; Madden et al., 2013; Bie and Ryder, 2014; Biasi and Wesnousky, 2016; Mildon et al., 2016). While modelled static Coulomb stress change on dip-slip receiver faults is highly sensitive to changes in fault strike, dip-slip faults also demonstrate sensitivity to changes in fault dip (Madden et al., 2013; Mildon et al., 2016; Mohammadi et al., 2019). Therefore, the ability to include down-dip changes in fault dip is important, particularly in fold and

thrust belts where faults are often interpreted to have ramp-flat geometry (e.g., Suppe, 1983; Shaw and Suppe, 1996; Hubbard et al., 2016; Levy et al., 2019) and where ramp-flat geometry can potentially control coseismic slip patterns (Hubbard et al., 2016). Furthermore, previous work has combined paleoseismic data and subsurface data with static Coulomb stress modeling to test feasible rupture scenarios between imbricate faults in the South Island, New Zealand (Stahl et al., 2016). However, in general, very few studies attempt to integrate field observations, surface data, and subsurface data in models of static Coulomb stress change to create more realistic representations of complex subsurface fault interactions.

This work focuses on the Ventura basin, southern California, USA to characterize the three-dimensional geometry of an active fault system using subsurface well-log data and then to investigate how static stress may be transferred along the fault network for different rupture scenarios. Several authors have suggested that large-magnitude (M_w 7.5–8.0) multi-fault earthquakes may occur between the Pitas Point, Ventura, and San Cayetano faults (Fig. 1) based on large coseismic uplift events inferred from paleoseismic studies, which imply a high degree of assumed structural connectivity between these faults at depth (Hubbard et al., 2014; McAuliffe et al., 2015; Rockwell et al., 2016). For example, four uplift events between 7–12 m are interpreted to have occurred on the Pitas Point fault at 6.70, 4.40, 2.09, and 0.95 ka based on analysis of uplifted marine terraces (Rockwell et al., 2016), and two uplift events of 5–6 m are suggested to have occurred on the Ventura fault at 4.4 ka and 0.24–0.80 ka based on shallow bore-hole and cone penetration tests (McAuliffe et al., 2015). Additionally, at least one 4–5 m slip event is suggested to have occurred on the eastern section of the San Cayetano fault at some point during the period 0.24–0.36 ka based on data from paleoseismic trenching (Dolan and Rockwell, 2001).

Alternatively, the prospect for multi-fault ruptures on these faults has been questioned by other researchers partly due to a lack of evidence for deep structural connectivity of Ventura basin faults in seismicity data and also partly due to the lack of evidence for synchronous fault displacement (Nicholson et al., 2017b). The timing of uplift events suggested from paleoseismic data implies that large-magnitude uplift events that occur on the Ventura fault may be synchronous with events on the San Cayetano fault but that large-magnitude uplift events on the Pitas Point fault do not necessarily

always occur on the Ventura fault just ~10 km to the east, and vice versa (Fig. 1). Sequences of large-magnitude earthquakes that are closely spaced in time are often associated with changes in static Coulomb stress (e.g., King et al., 1994). Additionally, events induced by laterally propagating changes in static Coulomb stress have previously been suggested as one possible mechanism to explain the potential mismatch in timing for large-magnitude events inferred along the Pitas Point, Ventura, and San Cayetano faults (McAuliffe et al., 2015). However, this suggestion has not been tested. Furthermore, the potential degree of multi-fault connectivity partly depends on the subsurface geometry of the Southern San Cayetano fault (SSCF) (Fig. 1) and the nature of its potential connection with the neighboring San Cayetano, Pitas Point, and Ventura faults, which remains unresolved (Hubbard et al., 2014; Hughes et al., 2018; Levy et al., 2019).

In this study, we examine petroleum industry well-log data and existing structural cross sections developed from well-log data, in conjunction with geologic maps, to produce a series of cross sections across the northern boundary of the central Ventura basin and to characterize the three-dimensional geometry of the low-angle SSCF. Using these data, we construct a three-dimensional model of the low-angle SSCF and compare the three-dimensional model to previous interpretations of the SSCF derived from structural modeling. We then use this complex thrust fault geometry in static Coulomb stress modeling using an updated method for creating variable-strike faults in *Coulomb 3*.4 (Mildon et al., 2016). The code was updated here to incorporate faults that change geometry both down-dip and along-strike i.e., to be able to model inferred ramp-flat fault geometry. The static Coulomb stress modeling explores whether subsequent earthquakes on the low-angle SSCF and the San Cayetano fault may be promoted by static Coulomb stress changes as a result of modelled ruptures on the Pitas Point or Ventura faults. The models also provide a framework for how simple static Coulomb stress modeling can be used in fold and thrust belts to forecast potential fault behavior in the absence of recent historical earthquake data.

2. Background and Geological setting

The Ventura basin is a deep, east-west trending, fault-bounded, structural trough that contains up to 12-km of Neogene sediments (e.g., Yeats et al., 1994). Rapid convergence across the basin is the result of

oblique transpressional deformation south of the "Big Bend" in the San Andreas fault (e.g., Wright, 1991), where geodetic studies suggest that current rates of shortening across the central and eastern basin range from 7–10 mm yr^{-1} (Donnellan et al., 1993; Marshall et al., 2013). High rates of shortening are accommodated along the northern Ventura basin by activity on the north-dipping Pitas Point, Red Mountain, Ventura, Southern San Cayetano, and San Cayetano faults, and the south-dipping Padre Juan, Lion Canyon, Big Canyon, Sisar, and Oak Ridge faults and associated folds (Fig. 1) (Namson and Davis, 1988; Rockwell, 1988; Yeats et al., 1988; Sorlien et al., 2000; Hubbard et al., 2014; Sorlien and Nicholson, 2015; Rockwell et al., 2016; Nicholson et al., 2017b; Hughes et al., 2018; Levy et al., 2019).

The Plio-Pleistocene stratigraphy of the Ventura basin consists of a progradational succession of deep marine to terrestrial strata that are highly deformed and locally overturned (Campbell et al., 2014). Various terminologies have been adopted to classify the Plio-Pleistocene sediments of the Ventura basin (Kew, 1924; Weber et al., 1976; Dibblee, 1990b; DeVecchio et al., 2012) and the nomenclature used in this study is based on a detailed synthesis of the existing literature (Campbell et al., 2014). The Plio-Pleistocene Pico Formation, is a 4-km thick succession of deep marine sandstone, siltstone, and mudstone, which is exposed along the north flank of the Santa Clara Valley (Fig. 1) (Winterer and Durham, 1962). The mudstone dominated Mudpit shale member of the upper Pico Formation interfingers with the overlying shallow marine sands of the lower Pleistocene Las Posas Formation, which is 100–300 m thick in the study area (Fig. 1). The youngest bedrock unit in the study area is the time-transgressive terrestrial Saugus Formation, which is thought to be Pleistocene in age (Levi and Yeats, 1993) and comprises a ~2-km thick succession of strongly deformed mudstone, siltstone, sandstone, and conglomerate (Fig. 1) (Hopps et al., 1992). Overlying the basin fill on the northern flank of the Santa Clara Valley is a series of uplifted and tilted late Pleistocene to Holocene alluvial fans and fluvial terraces (Rockwell, 1988; DeVecchio et al., 2012; Hughes et al., 2018).

The San Cayetano fault is an active reverse fault that defines the northern margin of the central Ventura basin and is mapped for ~40 km trending east-west from Piru to the Upper Ojai Valley (Fig. 1). The fault has been well documented both at the surface (Çemen, 1977; Rockwell, 1983; Rockwell, 1988; Çemen, 1989; Dibblee, 1990a; Dibblee, 1990b; Dolan and Rockwell, 2001) and in the subsurface

(Çemen, 1989; Hopps et al., 1992; Huftile and Yeats, 1995; Huftile and Yeats, 1996; Nicholson et al., 2007). The San Cayetano fault has two distinct segments with different geomorphic expression, which are separated by a pronounced bend in the surface trace north of the town of Fillmore (Fig. 1). In this study, the eastern segment of the San Cayetano fault is referred to as the eastern San Cayetano fault (ESCF). As the ESCF approaches the surface, the fault bifurcates into a low-angle 'Piru strand' with a dip of 10–30° and a 'main strand' that dips ~50° (Çemen, 1989; Huftile and Yeats, 1996). The Piru strand has pronounced geomorphic expression in the form of a 5–8 m high scarp in late Holocene (<5 ka) deposits near the town of Piru (Fig. 1), whereas no recent activity is thought to have occurred on the main strand (Dolan and Rockwell, 2001). The western segment of the San Cayetano fault is referred to here as the western San Cayetano fault (WSCF). There is a lack of prominent fault scarps in late Holocene deposits along the WSCF (Rockwell, 1988) and no paleoseismic data are available along the WSCF. The term San Cayetano fault is used here to refer to the combined WSCF and ESCF, which form a continuous surface below ~3 km depth (e.g., Cemen, 1989; Nicholson et al., 2017a).

Hughes et al. (2018) define the SSCF as a ~20 km long, low-angle thrust in the footwall of the WSCF. The SSCF has a slip rate of 1.3–1.9 mm yr^{-1} and is thought to have been active since ~58 ka based on the relative activity of flexural slip faults in the SSCF hanging wall, which are offset by the SSCF (Hughes et al., 2018). This previous work on the SSCF focused on surface evidence for the fault, but the subsurface three-dimensional geometry and structural connection of the SSCF with neighboring structures requires further investigation (Hughes et al., 2018). A north-dipping and a south-dipping model have also previously been suggested for the subsurface structure of the SSCF to explain the presence of a large fold limb in the footwall of the San Cayetano fault (Hubbard et al., 2014). However, limited field evidence and well data were provided in that study to support either of these previous models. The work presented here builds on the initial surface investigation and aims to explore the subsurface three-dimensional geometry and various proposed subsurface models for the SSCF in detail.

3. Datasets and Methods

3.1 Datasets

We integrated various surface and subsurface datasets to produce a series of structural cross sections along strike of the SSCF, to generate a three-dimensional model of the SSCF, and to investigate how the SSCF may connect with the San Cayetano and Ventura faults. The full set of data sources, including both well data and geological maps, is as follows:

- *California Department of Conservation (Division of Oil, Gas and Geothermal Resources or DOGGR) online well database:* A comprehensive online record of almost all historical oil wells drilled in California including, but not limited to, oil and gas production records, resistivity logs, drillers logs, paleontological data, and dipmeter data (herein referred to as 'the DOGGR online well database').

- *Ventura Basin Study Group well correlation sections*: The Ventura Basin Study Group (VBSG) provide a comprehensive review of the subsurface structure of the onshore Ventura basin comprising structural contour maps of key stratigraphic horizons and well-correlation sections across all major structures based on an integrated analysis of well data from 1200 petroleum industry wells (Hopps et al., 1992). Wells are typically tied or correlated in four directions, to create a grid of correlation sections that allows for a unified three-dimensional interpretation of subsurface structure and stratigraphy. Primary data extracted from the VBSG well correlation sections to characterize the SSCF included dipmeter data, dip data from core-logs, and resistivity data.
- *Existing structural cross sections:* In addition to the VBSG, several researchers have previously examined the subsurface structure of the study area and produced structural cross sections (Schlueter, 1976; Çemen, 1977; Huftile, 1988; Rockwell, 1988; Çemen, 1989). Cross sections and interpretations of well data included on the cross sections (if present) were re-interpreted to characterize the SSCF.
- *Geological maps:* Numerous geologic maps have been drafted in the study area (Dibblee, 1987; Dibblee, 1990a; Dibblee, 1990b; Dibblee and Ehrenspeck, 1992; Tan et al., 2004; Campbell et al.,

2014). Data on outcrop patterns, mapped folds and faults, along with strike and dip data were extracted from maps and used to aid cross section construction.

- *Geomorphic maps:* A sequence of uplifted alluvial terraces and offset alluvial fans have been mapped in the hanging wall of the SSCF and in the Upper Ojai Valley (Rockwell, 1983; Rockwell, 1988; DeVecchio et al., 2012; Hughes et al., 2018). These data helped quantify the surface expression of the SSCF to compare with results of the subsurface investigation.

3.2 Methods

The Ventura basin is a major onshore oil producing region and, consequently, oil wells are numerous throughout the study area (Fig. 1b). Wells drilled around Fillmore have an average maximum depth of 4–5 km, but wells on the southern slopes of Santa Paula Peak (Fig. 1) in the hanging wall of the SSCF are generally only 1–3 km deep. A north-dipping SSCF combined with an increase in elevation northward from the Santa Clara Valley, means that unless the fault was very low-angle (i.e., <5°) a large proportion of these wells would not be deep enough to penetrate the SSCF (Fig. 1). Furthermore, many of the wells in the hanging wall of the SSCF are inactive historical wells and the associated data are often limited. Consequently, out of approximately one thousand wells that could potentially penetrate the SSCF, only around fifty contain data (e.g., dipmeter readings, core-logs, or resistivity data) at the appropriate depth that can potentially be used to identify the low-angle SSCF. These fifty wells formed the basis for the SSCF interpretations in our study (Fig. 1b, red and orange dots).

3.2.1 Dipmeter data

With the onset of activity on the SSCF thought to have occurred within the last 58 kyr and with an inferred maximum surface slip rate of ~1.9 mm yr^{-1} (Hughes et al., 2018), the SSCF is expected to have accumulated a maximum displacement of ~110 m. Given such limited stratigraphic offset, methods of fault identification that rely solely on unambiguous identification of stratigraphic offsets in the subsurface (e.g., biostratigraphy or repetition of stratigraphy) may not be the most effective methods to identify the SSCF in well data. Disturbances in dipmeter trends are often associated with faulting and we interpret an abrupt change in dip, which can either be an abrupt decrease or increase in dip-angle with depth (or both if one follows the other), to represent potential evidence for a fault cut (where the

fault is interpreted to intersect the well) at or just below the change in dip (Devilliers and Werner, 1990; Adams et al., 1992; Hubbard et al., 2014). We focused primarily on disturbances in the dipmeter data at a depth corresponding to the trend of the low-angle SSCF suggested by Hughes et al. (2018), which was only based on data from two wells at Orcutt Canyon (Fig. 1).

We assume an uncertainty of up to 20° is associated with individual dipmeter readings and only changes in down-well dipmeter data above 20° are considered significant. Sediment compaction, rather than faulting, could also alter the geometry of beds and related dipmeter data with depth (Nicholson et al., 2007). However, down-well changes in dipmeter data that result from compaction would likely demonstrate a systematic, gradual change in bed geometry with depth, in contrast to a more abrupt down-well change in dipmeter data associated with faulting (Devilliers and Werner, 1990; Adams et al., 1992). Original, uninterpreted dipmeter data are only sporadically available in the DOGGR online well database within the study area, so we rely mainly on dip data included in existing correlation and structural cross sections that have been corrected for well drift from vertical and adjusted for the orientation of the cross section data panel (e.g., Schlueter, 1976; Huftile, 1988; Hopps et al., 1992).

3.2.2 Core logs

Many well records within the DOGGR online well database contain core logs that briefly describe the stratigraphy and note any specific features such as faults, fractures, gouge zones, slickensides, fossils, or traces of hydrocarbons. Core logs also contain dip data annotations ascertained from the orientation of bedding, sedimentary structures, or fractures within the core. Such annotated dip data from core logs are typically low resolution compared to the almost continuous readings from dipmeter data. However, changes in core-log dips were used to either support interpretations from dipmeter data or in place of dipmeter data if dipmeter data were not available. Core logs were also examined for any first-hand observations of faulting, such as pervasive fracture zones or gouge zones.

3.2.3 Resistivity data

Resistivity data are available for many wells in the study area from the DOGGR online well database. Fluid migration along the fault plane can affect the resistivity signal, while fault gouge and/or fractures

surrounding a fault zone can potentially cause the logging tool to fail (Hubbard et al., 2014). However, resistivity data alone from a single well are not normally used to suggest the presence of a fault (Devilliers and Werner, 1990). Sharp variations in resistivity have previously been used to support the identification of faults when they co-exist with other data that suggest the presence of a fault, for example dipmeter data (Devilliers and Werner, 1990). Changes in resistivity data, when they are observed at a depth roughly equal to the depth with abrupt variations in dip, were used to provide further supporting evidence for fault cuts related to the SSCF.

3.2.4 Well confidence categorization

The wells mapped in Figure 1b are color-coded based on a qualitative assessment of the degree of confidence with which the observations of possible fault cuts interpreted in the well data potentially provide evidence for the low-angle SSCF. Wells are classed as high-confidence if the inferred fault cut is based on multiple potential lines of evidence for faulting (e.g., a change in trend of dipmeter and on the resistivity logs) or if two wells are in close proximity and both show the same evidence for a fault cut (e.g., a disturbance on dipmeter data at similar depth) (Fig. 2). Direct evidence of a fault (e.g., a fault zone or a fault cut described in core logs) is considered to have higher confidence than an indirect indicator such as core-log dip data. Wells are assigned moderate confidence where the interpretation of the SSCF is based on one direct piece of evidence for the fault. Fault cuts in wells are assigned low confidence if there is some evidence for a fault in terms of subtle dip changes, but where we may expect the fault cut there are data missing.

3.2.5 Cross sections and three-dimensional fault model construction

We created three vertical structural cross sections (Fig. 3) and a three-dimensional fault model for the SSCF (Fig. 4) to map any potential along-strike variations in the two-dimensional and three-dimensional subsurface structure of the SSCF and to present our interpretation of how the SSCF intersects previously mapped structures and stratigraphy. Cross-section lines were selected to approximate the lines of section of the VBSG well-correlation sections within the study area (Hopps et al., 1992). The VBSG sections contain a large amount of well data corrected for well-bore deviation onto section lines. By constructing our cross sections in a similar orientation to the VBSG sections, the

cross sections followed the structural trend of the SSCF and the distance that well data needed to be projected onto the section was kept to a maximum of ~2 km. While this method does involve some (minor) projection of well data onto the line of cross-section (Fig. 1b), the wells used in construction of the three-dimensional model are not projected. Utilizing this method, the dip data contained in the VBSG sections could be used as a guide to model the subsurface geometry of the SSCF based on the fault cuts described in Table 1.

To construct the three-dimensional fault model of the SSCF, we georeferenced geological maps containing the well locations in the seismic interpretation software Petrel™. Fault intersections from the wells that we interpret to be related to activity on the SSCF were plotted as points and these points were gridded into a fault surface. The upper boundary of the fault surface was delineated using the mapped surface trace of the SSCF, which is amended here from Hughes et al. (2018) based on the results in section 4. The lower boundary was set as the intersection of the down-dip projection of the SSCF surface with the San Cayetano fault, based on our interpretation these faults are connected at depth (see section 6.1). The geometry for the San Cayetano fault was extracted from the Southern California Earthquake Center three-dimensional Community Fault Model (CFM) version 5.2 (Plesch et al., 2007; Nicholson et al., 2017a), a comprehensive representation of three-dimensional fault geometry based on geologic and seismologic evidence. The resulting surface was used as a template to reconstruct the three-dimensional geometry for the SSCF in static Coulomb stress modeling.

4. Characterizing the three-dimensional geometry of the SSCF

4.1 Fault evidence from well data

Correlation of interpreted fault cuts from several wells within the study area show clear evidence for the existence of a low-angle SSCF (Figs. 2 and 3). Descriptions of fault cuts that we interpret as ‘high’ confidence evidence for the low-angle SSCF are included in Table 1 and illustrated in Figure 2. Further descriptions of the fault cuts with ‘high’ confidence are included in the supporting information (Text S1) along with a description of fault cuts that we categorize as ‘moderate’ to ‘low’ confidence that provide evidence for the SSCF (Table S1).

4.2 Cross sections

The eastern extension of the SSCF is difficult to define because there are few dip data (core or dipmeter) in the upper 1–2 km from the numerous existing wells that would help to characterize the subsurface structure at the eastern end of the SSCF (Fig. 1b). Our interpretation for the SSCF involves a 15° north-dipping fault (Fig. 3a) that projects at constant dip to a surface fold in the Santa Clara Valley (Fig. 1b). This geometry is presented because there is no evidence for surface deformation in the many late Pleistocene and Holocene alluvial fans that cross the range front east of section B-B', which would be expected if the SSCF crops out at the range front or was blind in the shallow subsurface (Fig. 1). Furthermore, throw rates derived from a fault scarp within an alluvial fan at Orcutt Canyon (Fig. 1b) of $1.5\ ^{+0.3}/_{-0.2}$ mm yr^{-1} since ~19 ka overlap with uplift rates for a fold in the Santa Clara Valley floor (Fig. 1b) of $1.9\ ^{+0.6}/_{-0.4}$ mm yr^{-1} since ~17 ka (Hughes et al., 2018), which potentially indicates that uplift of both the fold and the scarp is occurring on the same structure.

A fault named the Pagenkopp fault has been previously mapped in the footwall of the WSCF, based on the interpretation of the Pico Formation being thrust over the Mudpit shale in resistivity logs (Figs. 2 and 3a) (Çemen, 1989; Hopps et al., 1992). Well 1 (Table 1) is the only well in the study area where the Pico Formation is interpreted to be thrust over the Mudpit shale. However, in many logs we note a section of disturbed dips at 400–500 m above our preferred SSCF that could be related to the Pagenkopp fault (Fig. 2 and 3b). Alternatively, this upper dip disturbance could be a separate structure to the Pagenkopp fault that runs parallel to the low-angle SSCF in the fault hanging wall (Fig. 3).

The low-angle SSCF in Figure 3c is characterized by interpreted fault cuts in four separate wells and has a suggested dip of ~18°. There are only two wells north of the range front towards the western end of the low-angle SSCF fault (wells 18 and 19) (Fig. 1). While these wells have insufficient data to provide evidence for the low-angle SSCF, we suggest the SSCF does extend this far west because faults have been observed in shallow boreholes drilled in late Pleistocene alluvial fans along the range front immediately south of the location of wells 18 and 19 (Earth Systems Southern California, 2013; Hughes et al., 2018). West of wells 18 and 19, the number of wells that could potentially penetrate the low-

angle SSCF but show no evidence of faulting increases (Fig. 1). Consequently, we suggest activity on the low-angle SSCF dies out 2–3 km west of wells 18 and 19 (Fig. 1).

4.3 Three-dimensional fault model

The three-dimensional model of the low-angle SSCF presented in Figure 4 encompasses all of the data presented in Figures 2 and 3 and in Table 1, in addition to the surface trace of the SSCF (c.f. Hughes et al., 2018). When the combined fault evidence from well data are plotted in their exact location and depth, the resulting fault surface can be defined by a continuous surface with an average dip of ~15° north that ranges in dip from 12–20°. The steepest dips occur in the center of the fault and the dip shallows slightly at the eastern and western ends (Fig. 4b). Owing mainly to a slight divergence in strike between the SSCF and the WSCF, the SSCF connects with the WSCF at a depth of ~1.5 km at its eastern end, which increases to ~3.5 km in the west (Fig. 4b).

The interpretation of the low-angle SSCF presented in Figure 4 is that it is not hard-linked with the Ventura fault and does not represent the eastward continuation of the Ventura fault or the Lion Canyon fault as previously proposed for a steeply dipping SSCF (Hubbard et al., 2014). The implications of the model for the low-angle SSCF presented in Figure 4 in terms of the broader structure and fault connectivity in the Ventura basin are discussed further in section 6.

5. Static Coulomb stress modeling

If the low-angle SSCF is not hard-linked with the Ventura fault, then the SSCF may not be as effective as a pathway for through-going ruptures between the Pitas Point, Ventura, and San Cayetano faults in large-magnitude multi-fault earthquakes as had been previously proposed (Hughes et al., 2018). Alternatively, static stress triggering has been suggested as one possible method for enabling multi-fault earthquakes between the Pitas Point, Ventura, and San Cayetano faults in response to a potential mismatch in the timing of large-magnitude uplift events inferred from paleoseismic data along these faults (McAuliffe et al., 2015). In the absence of evidence presented here for an effective dynamic rupture pathway, at least in the upper 7km, the aim of the static Coulomb stress modeling was to investigate the potential for triggered seismicity on various sections of the San Cayetano fault following

modeled large-magnitude earthquakes on the Pitas Point/Ventura fault. Our approach is similar to that of Stahl et al (2016) who used multiple hypothetical rupture scenarios and fault geometry in static Coulomb stress models to test the feasibility of specific rupture scenarios between two imbricate thrust faults.

5.1 Methods

The newly constructed three-dimensional geometry for the SSCF was used in static Coulomb stress modeling (Harris and Simpson, 1992; King et al., 1994; Harris, 1998; Parsons et al., 1999; Toda et al., 2005) using the software *Coulomb 3.4* (Lin and Stein, 2004; Toda et al., 2005). In our simple model, we assumed an initial stress of zero on all faults and simulated concentric ruptures on specific faults to observe patterns of modeled static Coulomb stress changes on the San Cayetano fault. No attempt was made to model dynamic stress effects or the current stress state of the faults resulting from historical ruptures (e.g., Deng and Sykes, 1997a, 1997b), interseismic loading (e.g., Verdecchia and Carena, 2016; Mildon et al., 2017; Wedmore et al., 2017), or cumulative transferred stress over a longer time period from post seismic relaxation of the lower crust and mantle (e.g., Freed et al., 2007). Dynamic stress models would require knowledge of frictional properties of the faults. Furthermore, both dynamic models and models for the current stress state of the fault would require an understanding of how an increase in shear modulus across the San Cayetano fault, due to the stiffness contrast between sediment and rock, will likely affect the magnitude of stress transferred from outside the Ventura basin to within the basin (Marshall et al., 2013). Constraining these factors is beyond the scope of the simple models conducted here.

5.1.1 Modeled fault surfaces

Faults were reconstructed in *Coulomb 3.4* (Lin and Stein, 2004; Toda et al., 2005) following the methodology of Mildon et al. (2016) for creating non-planar source and receiver fault inputs with variable strike. The original code for creating non-planar reverse faults in *Coulomb 3.4* only facilitated the modeling faults with variable strike and did not allow for modeling faults that change their geometry down-dip, a common feature of faults in fold and thrust belts (e.g., Shaw and Suppe, 1996). Accordingly, the code for creating non-planar reverse faults in *Coulomb 3*.4 was updated here to

incorporate faults that change geometry both down-dip and along-strike and, therefore, to model listric or ramp-flat fault geometry. The code is described in detail in Mildon et al (2016) and the updated version of the open source code is available from: https://github.com/ZoeMildon/three-dimensional-faults/tree/Variable_dip_faults.

The three-dimensional surface of the low-angle SSCF used in our model is based on the analysis of subsurface data presented in section 4. The Pitas Point, Ventura, and San Cayetano faults were reconstructed to produce a close match to fault surfaces included in CFM 5.2 (Fig. 5a) (Plesch et al., 2007; Nicholson et al., 2017a). Fault surface traces were loaded in Google Earth™ and traced over by hand. Faults were projected perpendicular to mean fault strike using a dip-profile that was based on the average dip of the fault surfaces included in CFM 5.2 (Fig. 5b) (Plesch et al., 2007; Nicholson et al., 2017a). The base of the seismogenic zone was taken to be 17 km in line with fault representations included in CFM 5.2 (Fig. 5c) (Plesch et al., 2007; Nicholson et al., 2017a).

Fault surfaces were modeled using rectangular elements with an along-strike element width of 1 km (Fig. 5c). Sensitivity analyses using along-strike element widths of 0.5 km, 1 km, and 2 km demonstrates almost no change in the distribution of static Coulomb stress change imparted on receiver faults or on maximum, minimum, and average values of static Coulomb stress change across the various sections of the San Cayetano fault (Fig. S1). A 1-km along-strike element width was selected to be consistent with the distribution of wells used in the 3D model of the low-angle SSCF (i.e., a well every ~1–2 km^2) and to obtain sufficient resolution while minimizing computational time.

Two alternative representations for the San Cayetano fault are presented in CFM 5.2 with 50° and 60° subsurface dips down to approximately 17 km (Nicholson et al., 2017a). Moreover, previous workers have matched shallow subsurface well-log data with deep seismicity to suggest a 40° subsurface dip for the San Cayetano fault (e.g., Huftile and Yeats, 1996). The intermediate value of 50° is adopted in our models as an average value between the two end members and we include the Piru strand of the upper ESCF in the model due to pronounced geomorphic expression associated with this strand (Fig. 5) (Dolan and Rockwell, 2001).

There is an ongoing discussion concerning the deep structure of the Pitas Point and Ventura faults (Hubbard et al., 2014; Marshall et al., 2017; Nicholson et al., 2017b; Levy et al., 2019). In the modeling conducted here, we adopt a ramp-flat-ramp geometry for the Pitas Point and Ventura faults (Fig. 5c) because this geometry shows a better fit to vertical geodetic data (Marshall et al., 2017; Hammond et al., 2018) when compared to alternative models which project the Pitas Point and Ventura faults to seismogenic depths at a relatively constant dip (Sorlien and Nicholson, 2015). However, results derived using alternative models are presented in the supplementary materials along with fault parameters used to construct fault surfaces in *Coulomb 3.4* (Table S2).

5.1.2 Model parameters

Static Coulomb stress change is defined by the following equation (Scholz, 1990):

$$\Delta\sigma_f = \Delta\tau + \mu'\Delta\sigma_n$$

where $\Delta\sigma_f$ is the static Coulomb stress change on the fault of interest, $\Delta\tau$ is the shear stress change, μ' is the effective coefficient of friction and incorporates pore pressure effects (e.g., Rice, 1992), and $\Delta\sigma_n$ is normal stress change. In the above equation, faults with a positive $\Delta\sigma_f$ after a nearby earthquake are hypothesized to be brought closer to failure and faults with negative $\Delta\sigma_f$ are thought to be moved away from failure.

During modeling an effective coefficient of friction of μ’ = 0.6 was applied. Sensitivity analysis for models using μ' values of 0.4, 0.6, and 0.8 demonstrate a systematic decrease in maximum, minimum, and average $\Delta\sigma_f$ with increasing μ' (Fig. S2). Moreover, the eastern half of the WSCF experiences positive $\Delta\sigma_f$ when a μ' of 0.4 is applied compared to mostly negative $\Delta\sigma_f$ across the whole fault plane when a μ' of 0.8 is employed (Fig. S2). A value of 0.6 is adopted here to be consistent with previous studies that modeled dynamic stress transfer in the Ventura basin and employed a μ' of 0.6 (Ryan et al., 2015). A μ' of 0.6 is also consistent with other models from southern California that have applied high values of μ' to thrust faults based on the sensitivity of thrust or reverse faults to changes in normal stress (Lin and Stein, 2004).

Coulomb 3.4 (Lin and Stein, 2004; Toda et al., 2005) uses a uniform elastic half-space and does not include gravitational effects because gravitational stresses are not needed to calculate static stress changes. Models presented here employed a Poisson's ratio of 0.25 and a shear modulus of 12 GPa. A shear modulus of 12 GPa has previously been applied to studies of stress transfer in the Los Angeles basin (Griffith and Cooke, 2004; Olson and Cooke, 2005), which is stratigraphically similar to the Ventura basin (Campbell et al., 2014). Modeled shear stresses are linearly related to fault slip, therefore, doubling the shear modulus would double the magnitude of resultant stresses imparted on receiver faults (assuming a constant Poisson's ratio).

In the absence of large recent historical earthquakes and associated published slip distributions on the Pitas Point, Ventura, or San Cayetano faults, data are limited to quantify the precise direction of fault slip during large earthquake ruptures on these faults. Many faults in the Ventura basin are thought to be oblique-reverse faults that include a significant component of left-lateral slip (Yerkes et al., 1987; Sorlien et al., 2000; Marshall et al., 2013). However, there is little geomorphological evidence, such as offset river channels or shutter ridges along either the Ventura, Southern San Cayetano, or San Cayetano faults to indicate a long-term component of strike-slip displacement on these faults (Hughes et al., 2018). Due to the uncertainty in the direction of fault slip during large earthquakes, we present results for two endmember models using rakes of 90° (pure dip-slip displacement) and 45° (oblique left-lateral ruptures with a 50/50 ratio of dip-slip to left-lateral slip) (Figs. 6 and 7).

5.1.3 Coseismic ruptures

We calculated maximum potential earthquake magnitude (M_w) for a specific fault using functions derived from regressions of M_w versus fault area (Leonard, 2014) and then model maximum slip on the fault to output the expected M_w from fault area (Table S3). The magnitude of $\Delta\sigma_f$ scales linearly with fault slip, therefore, changing the amount of slip on the fault will affect the magnitude of $\Delta\sigma_f$ but not the positive or negative patterns of $\Delta\sigma_f$ observed on receiver faults, assuming all other parameters are kept constant.

Sensitivity analysis with the location of maximum slip located in the southeast, southwest, northeast, and northwest sections of the Ventura fault demonstrate no significant change in the pattern of $\Delta\sigma_f$ on the WSCF receiver fault surface (Fig. S3). However, ruptures modeled along the eastern side of the Ventura fault result in greater magnitude maximum positive, minimum negative, and average $\Delta\sigma_f$ values compared to ruptures modeled on the western side of the Ventura fault. The variation is due to the closer proximity of ruptures modeled on the eastern Ventura fault to the WSCF, when compared to ruptures modeled on the western Ventura fault (Fig. S3). Changing the location of maximum slip in this way would not significantly alter any conclusions based on the model results.

Our preferred models were kinematic models with maximum slip modelled at the center of the fault (lengthwise and depth-wise) and a linear slip gradient that tapers to zero at the eastern and western fault tips and the base of the fault (Mildon et al., 2017). Both the Pitas Point and Ventura faults are blind (Hubbard et al., 2014; Sorlien and Nicholson, 2015). Therefore, both the Ventura fault and the Pitas Point fault are modelled with slip tapering to zero at the surface.

5.2 Model results

When pure dip-slip ruptures are simulated on the Ventura fault, the western half of the WSCF experiences mostly negative $\Delta\sigma_f$ with a maximum negative value of -3.23 bars (Fig. 6a). In contrast, the ESCF experiences positive $\Delta\sigma_f$ with a maximum positive value of 0.13 bars and the low-angle SSCF experiences mostly positive $\Delta\sigma_f$ with a maximum positive value of 0.91 bars (Fig. 6a). Pure dip-slip ruptures simulated on the Pitas Point fault result in small positive $\Delta\sigma_f$ across all sections of the San Cayetano fault with a maximum value of 0.25 bars on the WSCF (Fig. 6b). The sharp change from positive to negative $\Delta\sigma_f$ observed on the Ventura fault is a result of the abrupt increase in modeled fault dip from 25° to 50° (Fig. 6b). When both pure dip-slip and oblique left-lateral ruptures are simulated on the entire Pitas Point/Ventura fault, patterns of $\Delta\sigma_f$ are similar to the models with the Ventura fault as the source fault but with slightly higher values of $\Delta\sigma_f$ (Fig. 6c and 7c). For pure dip-slip ruptures of the entire Pitas Point/Ventura fault, the WSCF experiences negative $\Delta\sigma_f$ with a maximum negative

value of -2.72 bars, the SSCF experiences maximum positive $\Delta\sigma_f$ of 1.15 bars, and the ESCF experiences positive $\Delta\sigma_f$ with a maximum value of 0.26 bars (Fig. 6c).

When oblique left-lateral ruptures are simulated on the Ventura fault, the WSCF experiences strong negative $\Delta\sigma_f$ with a maximum negative value of -4.66 bars (Fig. 7a). The ESCF experiences positive $\Delta\sigma_f$ with a maximum positive value of 0.40 bars and the low-angle SSCF experiences mostly positive $\Delta\sigma_f$ with a maximum positive value of 1.00 bar (Fig. 7a). Oblique left-lateral ruptures simulated on the Pitas Point fault result in a complex pattern of positive and negative $\Delta\sigma_f$ across the WSCF with an average value of 0.11 bars across the fault surface (Fig. 7b). The ESCF records positive $\Delta\sigma_f$ with a maximum value of 0.31 bars and the low-angle SSCF records a maximum positive $\Delta\sigma_f$ of 0.61 bars (Fig. 7b). When oblique left-lateral ruptures are simulated on the entire Pitas Point/Ventura fault, the WSCF experiences negative $\Delta\sigma_f$ with a maximum negative value of -5.13 bars, the SSCF experiences maximum positive $\Delta\sigma_f$ of 1.59 bars, and the ESCF experiences positive $\Delta\sigma_f$ with a maximum value of 0.95 bars (Fig. 7c). The locations of maximum positive (stars) and maximum negative (diamonds) $\Delta\sigma_f$ on the receiver fault planes are shown in Figures 6 and 7, and all values for the maximum positive, maximum negative, and average $\Delta\sigma_f$ imparted on the various sections of the San Cayetano fault for the various earthquake rupture scenarios explored are included in supporting information (Table S4).

6. Discussion and implications

The following discussion section compares the model for the low-angle SSCF presented in Figure 4 with the previous models of derived geometry for the SSCF and the implications for the structural evolution and earthquake hazards of the Ventura basin. Additionally, the results of the static Coulomb stress models are used to investigate how large-magnitude earthquakes on the Pitas Point and Ventura faults may affect the earthquake behavior of the San Cayetano fault.

6.1 Geometry of the Southern San Cayetano fault

In Figures 3 and 4, the low-angle SSCF is interpreted to connect with the WSCF because the nearest well with a fault cut that was used to construct the 3D model of the low-angle SSCF is located just 1-

km south of the WSCF surface trace in the WSCF footwall (Well 2, Fig. 3a). Moreover, several other wells that were used to construct the 3D model are located in the hanging wall of the WSCF at the surface (Fig. 1c). In addition, the low-angle SSCF has much smaller surface area than the WSCF (Fig. 5a), but the slip rate for the low-angle SSCF of $1.3\ ^{+0.5}/_{-0.3}$ mm yr^{-1} since 7.3 ka (Hughes et al., 2018) is similar to the slip rate of 1.4 $^{+}/_{-}$ 0.4 mm yr^{-1} since 8–10 ka for the WSCF (Rockwell, 1988). A contrasting fault area but similar slip rate is consistent with the hypothesis that the SSCF and the WSCF may be kinematically and structurally linked in the subsurface. Consequently, the low-angle SSCF is interpreted as a low-angle footwall splay which connects to the WSCF in the upper 1.5–3.5 km (Fig. 4).

Two initial, more steeply-dipping models were first proposed for the SSCF to account for a large south-dipping fold limb mapped in the footwall of the WSCF along the northern margin of the Santa Clara Valley (Fig. 8a) (Hubbard et al., 2014). One model (model 1) presents the SSCF as the eastward extension of the Lion Canyon fault which forms a ~60° south-dipping back-thrust off a sub-horizontal detachment surface at ~7 km depth (Fig. 8b). The alternative geometry (model 2) is a 45–55° north-dipping eastward extension of the Ventura fault, which soles out onto a sub-horizontal detachment at ~7 km depth (Fig. 8c) (Hubbard et al., 2014). The low-angle SSCF presented here is based on a comprehensive review of available well data in the footwall of the San Cayetano fault and does not match either of the initial models proposed for the SSCF (Fig. 8d). In Well 1, a possible fault zone is recorded on a core log at a depth of 2920 mbsl (Fig. 3a). If this inferred fault zone was projected to our surface trace of the SSCF, it would define a ~45° north-dipping fault, similar to model 2 for the original proposed SSCF (Fig. 8c) (Hubbard et al., 2014). However, the 45° north-dip model is discounted because no other wells investigated in this study provide evidence for such a structure.

Based on surface data, the SSCF may have accumulated a maximum of 110 m of dip-slip separation. While dip-slip separation could potentially increase with depth, it is unlikely that the low-angle SSCF has accumulated sufficient slip to account for the south-dipping fold limb in the footwall of the WSCF because the fold limb is at least 5 km wide in the study area and must have accommodated significant shortening (Fig. 1). Furthermore, we interpret the low-angle SSCF to cut through the south-dipping fold limb (Fig. 3), which indicates that the low-angle SSCF probably postdates the fold limb.

The fault referred to as the 'Lion fault' in the initial models for the SSCF (Hubbard et al, 2014) is in fact three separate faults: the Sisar, Lion Canyon, and Big Canyon faults (Fig. 3) (Huftile, 1988; Hopps et al, 1992; Huftile and Yeats, 1995). These faults form a 30-km long, east-west striking, south-dipping, fault system which is mapped at the surface from the western end of Sulphur Mountain (Fig. 1) to just east of Timber Canyon (Dibblee, 1987; Dibblee, 1990b; Huftile, 1988; Yeats and Huftile, 1995). In the subsurface, the Lion Canyon fault is not mapped east of section C–C' where the Lion Canyon fault is truncated against the WSCF (Fig. 3c). The Sisar fault is mapped at the surface and in the subsurface in the footwall of the San Cayetano fault for ~5 km east of section B–B', where it thrusts Miocene rocks above Pliocene Pico Formation (Fig. 3b) (Dibblee, 1990b; Hopps et al., 1992). The continuation of the south-dipping fault-system in the footwall of the WSCF supports the south-dipping model 1 for the original SSCF (Hubbard et al., 2014). Furthermore, with ~1–2 km of combined dip-slip displacement (Fig. 3c), the south-dipping fault system could be the fault system responsible for the south-dipping fold limb. However, if the south-dipping fold limb in the footwall of the WSCF is linked to slip on the Sisar and Lion Canyon faults, then this should not be referred to as the SSCF because the eastward continuation of the south-dipping faults has previously been referred to as the Sisar fault (Dibblee, 1990b; Yeats and Huftile, 1995). Given that the interpretation of the low-angle SSCF presented in Figures 3 and 4 is that it is connected to the WSCF, we suggest that the low-angle SSCF should herein be referred to as the SSCF.

There is ongoing debate about whether the Sisar, Lion Canyon, and Big Canyon faults sole out onto a gently south-dipping surface at ~7 km beneath the Ventura basin (Nicholson et al, 2017b) or whether they form a back-thrust off some form of gently north-dipping blind fault (Levy et al., 2019). The well data presented in this study has a maximum depth of ~5 km (Fig. 3) and does not provide direct evidence to support either interpretation. Regardless of the deep structure of the south-dipping faults, the Lion Canyon and Sisar faults are thought to be inactive, or at least no longer active at the surface, due to a lack of surface scarps associated with the fault trace (Hughes et al., 2018). A lack of surface scarps is the reason for the interpretation that the Lion Canyon and Sisar faults are offset by the SSCF in Figure 3.

6.2 Static Coulomb stress interactions

The interpretation of the SSCF presented here indicates that the SSCF is not hard linked to the Ventura fault. We note, however, that well data are limited in the area between the eastern end of the Ventura fault and the western end of the SSCF, and so data are lacking to precisely model this fault intersection. If the SSCF is not connected to the Ventura fault, the SSCF may not be as effective a pathway for through-going ruptures between the Pitas Point/Ventura and San Cayetano faults as previously suggested (Hughes et al., 2018).

Through-going ruptures are thought to occur between the Pitas Point, Ventura, and San Cayetano faults due to large-magnitude uplift events inferred in paleoseismic studies (Dolan and Rockwell, 2001; McAuliffe et al., 2015; Rockwell et al., 2016). If such ruptures do occur, they would need to propagate between the faults at depth along blind ramp structures such as those suggested by kinematic structural modeling (Hubbard et al, 2014; Levy et al., 2019), cross section balancing (Namson and Davis, 1988; Huftile and Yeats, 1995, 1996), and mechanical modeling based on GPS data (Marshall et al., 2017; Hammond et al, 2018). However, in the absence of a confirmed through-going rupture pathway identified in the well data, here we use the results of the static Coulomb stress modeling to investigate how proposed large-magnitude earthquakes on the Pitas Point and Ventura faults may influence subsequent seismicity on the San Cayetano and Southern San Cayetano faults, via static Coulomb stress transfer. Models of static Coulomb stress change have previously been utilized to understand the kinematics for the multi-fault rupture sequence during the 2010 M_w 7.1 Darfield earthquake, New Zealand (Quigley et al., 2019) and to test the feasibility of various rupture scenarios between the Fox Creek and Fox Peak faults on the South Island of New Zealand (Stahl et al., 2016).

Large to moderately sized earthquakes (i.e., $M_w > 6$) generally nucleate at depths near the base of the seismogenic zone and faults present in the upper 3 km of the crust, such as the SSCF, are not capable of storing sufficient elastic strain energy to generate large earthquakes (e.g., Das and Scholz, 1983). Consequently, any large earthquake that propagates to the surface on the SSCF would probably nucleate at depth on the lower San Cayetano fault, to which the SSCF is connected at 2–4 km depth (Fig. 4). In most models, the strongest signal on the San Cayetano fault is a large area of negative $\Delta\sigma_f$ of >1 bar

across the western half of the WSCF surface (Figs. 6 and 7). The patch of negative $\Delta\sigma_f$ indicates that the likelihood of triggered events on the WSCF may be decreased by large-magnitude events on the Pitas Point and Ventura faults (Figs. 6 and 7). Stress heterogeneities on a fault surface can inhibit rupture propagation across the fault surface (Steacy and McCloskey, 1998; Mildon et al., 2017). Therefore, even if the Ventura and San Cayetano faults are connected by some sort of deep ramp structure in the subsurface (Hubbard et al, 2014; Levy et al., 2019), strong negative $\Delta\sigma_f$ on the WSCF brought on by earthquakes on the Pitas Point or Ventura faults could potentially act as a stress barrier to rupture propagation along strike. A potential stress barrier on the WSCF may partly explain why several large-magnitude uplift events on the Pitas Point and Ventura faults suggested from paleoseismic studies are not also observed on the San Cayetano fault (Dolan and Rockwell, 2001; McAuliffe et al., 2015; Rockwell et al., 2016).

In contrast to the WSCF, the ESCF and the SSCF experience mostly positive $\Delta\sigma_f$ in all of the models and the magnitude of $\Delta\sigma_f$ is generally largest for the models that assume left-lateral oblique slip on the Pitas Point and Ventura faults (Figs. 6 and 7). The value of $\Delta\sigma_f$ that represents a triggering threshold (i.e., changes above which are thought to be sufficient to trigger seismicity) is poorly understood, with estimates ranging from 1 bar (Kilb et al., 2002), 0.5 bars (King et al., 1994), and 0.2 bars (Toda et al., 1998), to values as low as 0.01 bars (Rydelek and Sacks, 1999; Ziv and Rubin, 2000; Ogata, 2005). Furthermore, heterogeneities in the strength of the fault (Harris and Day, 1999) or in the stress state of the fault prior to rupture (Ben-Zion and Sammis, 2003) can dictate whether a triggered event occurs on a receiver fault, neither of which have been quantified here. Despite these uncertainties, for ruptures modeled on the Pitas Point and Ventura faults the maximum positive $\Delta\sigma_f$ values ranging from 0.03–0.10 bars on the lower ESCF for the pure dip-slip models and 0.40–0.95 bars in the left-lateral oblique slip models could, in theory, cascade into a subsequent event on the ESCF.

A contrast in geomorphic expression between the ESCF and the WSCF may partly be a product of the different $\Delta\sigma_f$ imparted across the San Cayetano fault from ruptures on the Pitas Point and Ventura faults. Specifically, the 5–8 m high scarp in late Holocene (<5 ka) alluvial deposits along the ESCF

(Dolan and Rockwell, 2001) may be a reflection of a higher likelihood of ruptures nucleating on the ESCF due to positive $\Delta\sigma_f$ resulting from preceding events on the Pitas Point or Ventura faults. Conversely, the lack of pronounced fault scarps in late Holocene alluvial surface along the WSCF may result from relatively less frequent events on WSCF due to negative $\Delta\sigma_f$ brought on by earthquakes on the Pitas Point and Ventura faults.

A source of uncertainty in the $\Delta\sigma_f$ models is the deep geometry of the Pitas Point and Ventura faults. The models in Figures 6 and 7 adopt a ramp-flat-ramp geometry for the Pitas Point/Ventura fault. This subsurface model is based primarily on two-dimensional kinematic modeling, shallow onshore seismic reflection data, and limited well control (Hubbard et al., 2014). However, in an alternative model, the Pitas Point and Ventura faults maintain a relatively constant dip down to ~10 km depth where they merge with the Red Mountain and Arroyo-Parida faults to form a master north-dipping fault that continues with moderate-to-steep dip to seismogenic depths of 18–20 km (Sorlien and Nicholson, 2015; Nicholson et al., 2017b). The deep geometry of the alternative model is based on correlating well data and offshore two-dimensional and three-dimensional seismic reflection data with deep seismicity (Nicholson et al., 2017b). If the alternative model is adopted for the Pitas Point and Ventura faults and dip-slip ruptures are simulated on the Pitas Point fault, then slight positive $\Delta\sigma_f$ is recorded across most of the WSCF and the SSCF (Fig. S5), similar to the results for the ramp-flat-ramp model (Figs. 6b). If the alternative model is adopted and dip-slip ruptures are simulated on the Ventura fault, then negative $\Delta\sigma_f$ is recorded on the lower section of the WSCF (Fig. S5) and like in the ramp-flat-ramp geometry models (Fig. 6), the prospect of triggered seismicity is decreased. Therefore, adopting this alternative model for the Pitas Point and Ventura faults will probably not change the conclusions of this discussion.

The focus of this study is the Pitas Point, Ventura, Southern San Cayetano, and San Cayetano faults because these faults all have pronounced geomorphic expression and/or paleoseismic data. Including other proximal faults such as the Oak Ridge, Simi, Red Mountain, Padre Juan, and Arroyo-Parida faults (Figs. 1 and 5a) in the models but not simulating ruptures on them does not change $\Delta\sigma_f$ recorded on the San Cayetano fault as a result of ruptures on the Pitas Point or Ventura faults. However, earthquakes on the faults not modeled here would obviously influence the current stress state of the San Cayetano fault.

Moreover, the potential stress changes induced by large magnitude events on the San Andreas fault (e.g., Deng and Sykes, 1997a) and long-term stresses due to plate boundary interactions (Freed et al., 2007) would also play an important role in controlling the current stress state of faults in the Ventura basin. Further work should attempt to model these various important parameters for the Ventura basin.

6.3 Ground rupture hazard of the SSCF

Regardless of the exact mechanism for earthquake nucleation, ruptures that nucleate on the lower San Cayetano fault may sometimes propagate to the surface along the SSCF rather than continue up-dip along the central section of the upper WSCF. The pattern of ruptures preferentially travelling up-dip from depth along low-angle reverse faults near the surface has previously been documented on the ESCF (Dolan and Rockwell, 2001). The Piru strand of the ESCF exhibits a 5–8 m high multi-event scarp in late Holocene alluvial fans whereas the main strand is thought to be inactive and demonstrates no evidence of Holocene or recent activity (Dolan and Rockwell, 2001).

Dynamic rupture simulations of slip propagating up-dip over a decrease in fault dip show that slip is increased on low-angle sections of faults due to dynamic unclamping and decreased normal stress on the low-angle fault (Ryan et al., 2015). Dynamic unclamping, in combination with the positive $\Delta\sigma_f$ recorded on the ~15° SSCF in all the earthquake rupture scenarios tested here (Figs. 6 and 7) suggest that ruptures may preferentially propagate to the surface along the SSCF. This appears to be supported by evidence from geomorphology because a fault scarp with ~9 m of vertical separation is recorded in a 7.3 ka alluvial terrace that crosses the SSCF (Hughes et al., 2018). There are no fault scarps observed in Holocene surfaces that cross the section of the WSCF in the hanging wall of the SSCF. However, fan head segmentation of a late Holocene (<5 ka) alluvial fan has been attributed to surface activity on the WSCF (Rockwell, 1988). Therefore, ruptures may occasionally also propagate to the surface along the central WSCF or a combination of the SSCF and the WSCF.

7. Conclusions

Results from an integrated analysis of well data, geological maps, and cross sections help document the three-dimensional geometry of the low-angle Southern San Cayetano fault (SSCF) and reveal evidence

for the potential subsurface connection of the SSCF with the San Cayetano fault. The geometry of the low-angle SSCF derived from well-data differs from both of the previous models for the SSCF, which were derived from structural modeling to explain the presence of a large south-dipping fold limb in the footwall of the San Cayetano fault. Ruptures that nucleate at depth on the San Cayetano fault may sometimes propagate up-dip along the SSCF rather than the steeper upper section of the central San Cayetano fault, which potentially makes the SSCF a significant ground rupture hazard in the highly populated Santa Clara Valley.

The newly constructed fault model for the low-angle SSCF was employed in static Coulomb stress modeling using ramp-flat faults. Model results indicate that earthquakes on the Pitas Point and Ventura faults may decrease the likelihood of subsequent earthquakes on the western section of the San Cayetano fault (WSCF) but increase the likelihood of subsequent events on the eastern section of the San Cayetano fault (ESCF) and the SSCF. These results may partly explain contrasting geomorphic expression between the ESCF and the WSCF, and why the timings of large-magnitude uplift events on the Pitas Point and Ventura faults differ from the timing of large-magnitude uplift events recorded on the ESCF. In addition to new insights into the structure and earthquake behavior of the San Cayetano fault, a major seismically active reverse fault in southern California, the modeling presented here adds to a growing body of work to understand how static Coulomb stress models can be used to forecast potential fault behavior on complex geometry faults.

Acknowledgements

Well data were taken from the online database provided by the California Department of Conservation, Division of Oil, Gas, and Geothermal Resources website which is freely available at: https://gis-california.opendata.arcgis.com/datasets/cadoc::well-finder (last accessed January 2020). Work supported by funding from Southern California Earthquake Center (SCEC) award numbers 15100 (to DHR and DDV), 17184 (to DHR), 16049 (to TKR), and 17024 (to TKR). Additional funding was supplied by a Royal Geological Society postgraduate research grant (to AH), an Imperial College Janet Watson bursary (to AH), and a postgraduate research grant from the British Society for Geomorphology (to AH). The authors would also like to thank Schlumberger for providing usage of the software Petrel™

along with Judith Hubbard, Michele Cooke, and Mark Quigley for thoughtful comments and reviews on the manuscript. This is SCEC contribution number #10025.

References

Adams, J., Ayodele, J., Bedford, J., Kaars-Sijpesteijn, C. and Watts, N., 1992. Application of dipmeter data in structural interpretation, Niger Delta. Geological Society, London, Special Publications, 65(1): 247-263.

Beavan, J., Motagh, M., Fielding, E.J., Donnelly, N., Collett, D., 2012. Fault slip models of the 2010-2011 Canterbury, New Zealand, earthquakes from geodetic data and observations of postseismic ground deformation. New Zeal. J. Geol. Geophys. 55, 207–221.

Ben-Zion, Y., Sammis, C.G., 2003. Characterization of fault zones. Pure Appl. Geophys. 160, 677–715. https://doi.org/10.1007/PL00012554

Biasi, G.P. and Wesnousky, S.G., 2016. Steps and gaps in ground ruptures: Empirical bounds on rupture propagation. Bulletin of the Seismological Society of America, 106(3): 1110-1124.

Biasi, G.P. and Wesnousky, S.G., 2017. Bends and Ends of Surface Ruptures. Bulletin of the Seismological Society of America, 107(6): 2543-2560.

Bie, L. and Ryder, I., 2014. Recent seismic and aseismic activity in the Ashikule stepover zone, NW Tibet. Geophysical Journal International, 198(3): 1632-1643.

Campbell, R.H., Wills, C.J., Irvine, P.J. and Swanson, B.J., 2014. Preliminary geologic map of the Los Angeles 30'x 60' quadrangle, Southern California, 1: 100,000.

Candela, T., Renard, F., Schmittbuhl, J., Bouchon, M. and Brodsky, E.E., 2011. Fault slip distribution and fault roughness. Geophysical Journal International, 187(2): 959-968.

Çemen, I., 1989. Near-surface expression of the eastern part of the San Cayetano Fault: A potentially active thrust fault in the California Transverse Ranges. Journal of Geophysical Research, 94(B7): 9665-9677.

Clark, K., Nissen, E., Howarth, J., Hamling, I., Mountjoy, J., Ries, W., Jones, K., Goldstien, S., Cochran, U. and Villamor, P., 2017. Highly variable coastal deformation in the 2016 Mw 7. 8 Kaikōura earthquake reflects rupture complexity along a transpressional plate boundary. Earth and Planetary Science Letters, 474: 334-344.

Das, S. and Scholz, C., 1983. Why large earthquakes do not nucleate at shallow depths. Nature, 305(5935): 621-623.

Deng, J. and Sykes, L.R., 1997a. Evolution of the stress field in southern California and triggering of moderate-size earthquakes: A 200-year perspective. Journal of Geophysical Research: Solid Earth, 102(B5): 9859-9886.

Deng, J. and Sykes, L.R., 1997b. Stress evolution in southern California and triggering of moderate-, small-, and micro-size earthquakes. Journal of Geophysical Research: Solid Earth, 102(B11): 24411-24435.

DeVecchio, D.E., Heermance, R.V., Fuchs, M. and Owen, L.A., 2012. Climate-controlled landscape evolution in the Western Transverse Ranges, California: Insights from Quaternary geochronology of the Saugus Formation and strath terrace flights. Lithosphere, 4(2): 110-130.

Devilliers, M. and Werner, P., 1990. Example of fault identification using dipmeter data. Geological Society, London, Special Publications, 48(1): 287-295.

Dibblee, T., 1987. Geologic map of the Ojai Quadrangle, Ventura County, California, map number DF-13, 1: 24, 000. Dibblee Geological Foundation, Santa Barbara, California.

Dibblee, T., 1990a. Geologic map of the Fillmore quadrangle, Ventura County, California, map number DF-27, 1: 24,000. Dibblee Geological Foundation, Santa Barbara, California.

Dibblee, T., 1990b. Geologic map of the Santa Paula Peak quadrangle, Ventura County, California, map number DF-26, 1: 24,000. Dibblee Geological Foundation, Santa Barbara, California.

Dibblee, T.W. and Ehrenspeck, H.E., 1988a. Geologic map of the Ventura and Pitas Point quadrangles, Ventura County, California, 1: 24, 000. Dibblee Geological Foundation, Santa Barbara, California.

Dibblee, T.W. and Ehrenspeck, H.E., 1992b. Geologic Map of the Saticoy quadrangle: Ventura County, California, 1: 24, 000. Dibblee Geological Foundation, Santa Barbara, California.

Dolan, J.F. and Rockwell, T.K., 2001. Paleoseismologic evidence for a very large (M-w > 7), post-AD 1660 surface rupture on the eastern San Cayetano fault, Ventura County, California: Was this the elusive source of the damaging 21 December 1812 earthquake? Bulletin of the Seismological Society of America, 91(6): 1417-1432.

Douilly, R., Oglesby, D.D., Cooke, M.L., Hatch, J.L., 2020. Dynamic models of earthquake rupture along branch faults of the eastern San Gorgonio Pass region in California using complex fault structure. Geosphere 16, 474–489. https://doi.org/10.1130/ges02192.1

Earth Systems Southern California, 2013. Geo-Technical Feasibility Report for tract 5475, Santa Paula.

Fletcher, J.M., Oskin, M.E. and Teran, O.J., 2016. The role of a keystone fault in triggering the complex El Mayor-Cucapah earthquake rupture. Nature Geoscience, 9(4): 303-307.

Fletcher, J.M., Teran, O.J., Rockwell, T.K., Oskin, M.E., Hudnut, K.W., Mueller, K.J., Spelz, R.M., Akciz, S.O., Masana, E. and Faneros, G., 2014. Assembly of a large earthquake from a complex fault system: Surface rupture kinematics of the 4 April 2010 El Mayor–Cucapah (Mexico) Mw 7.2 earthquake. Geosphere, 10(4): 797-827.

Freed, A.M., 2005. Earthquake triggering by static, dynamic, and postseismic stress transfer. Annu. Rev. Earth Planet. Sci., 33: 335-367.

Freed, A.M., Ali, S.T. and Bürgmann, R., 2007. Evolution of stress in Southern California for the past 200 years from coseismic, postseismic and interseismic stress changes. Geophysical Journal International, 169(3): 1164-1179.

Griffith, W. and Cooke, M., 2004. Mechanical validation of the three-dimensional intersection geometry between the Puente Hills blind-thrust system and the Whittier fault, Los Angeles, California. Bulletin of the Seismological Society of America, 94(2): 493-505.

Hamling, I.J., Hreinsdóttir, S., Clark, K., Elliott, J., Liang, C., Fielding, E., Litchfield, N., Villamor, P., Wallace, L. and Wright, T.J., 2017. Complex multifault rupture during the 2016 Mw 7.8 Kaikōura earthquake, New Zealand. Science, 356(6334): eaam7194.

Harris, R.A., 1998. Introduction to special section: Stress triggers, stress shadows, and implications for seismic hazard. Journal of Geophysical Research: Solid Earth, 103(B10): 24347-24358.

Harris, R.A. and Simpson, R.W., 1992. Changes in static stress on southern California faults after the 1992 Landers earthquake. Nature, 360(6401): 251-254.

Harris, R.A., Day, S.M., 1999. Dynamic 3D simulations of earthquakes on en echelon faults. Geophys. Res. Lett. 26, 2089–2092. https://doi.org/10.1029/1999GL900377

Hauksson, E., Andrews, J., Plesch, A., Shaw, J.H. and Shelly, D.R., 2016. The 2015 Fillmore earthquake swarm and possible crustal deformation mechanisms near the bottom of the Eastern Ventura basin, California. Seismological Research Letters, 87(4): 807-815.

Hopps, T., E, Stark, H., E and Hindle, R., J, 1992. Subsurface geology of Ventura Basin, California, Ventura Basin Study Group Report. Rancho Energy Consultants, Inc, Santa Paula, California.

Hubbard, J., Shaw, J.H., Dolan, J., Pratt, T.L., McAuliffe, L. and Rockwell, T.K., 2014. Structure and Seismic Hazard of the Ventura Avenue Anticline and Ventura Fault, California: Prospect for Large, Multisegment Ruptures in the Western Transverse Ranges. Bulletin of the Seismological Society of America, 104(3): 1070-1087.

Hubbard, J., Almeida, R., Foster, A., Sapkota, S.N., Bürgi, P., Tapponnier, P., 2016. Structural segmentation controlled the 2015 MW 7.8 Gorkha earthquake rupture in Nepal. Geology 44, 639–642. https://doi.org/10.1130/G38077.1

Huftile, G.J., 1988. Geologic structure of the Upper Ojai Valley and Chaffee Canyon areas, Ventura County, California. Masters Thesis, Oregon State University, Corvallis, Oregon.

Huftile, G.J. and Yeats, R.S., 1995. Convergence rates across a displacement transfer zone in the western Transverse Ranges, Ventura basin, California. Journal of Geophysical Research: Solid Earth, 100(B2): 2043-2067.

Huftile, G.J. and Yeats, R.S., 1996. Deformation rates across the Placerita (Northridge Mw= 6.7 aftershock zone) and Hopper Canyon segments of the western Transverse Ranges deformation belt. Bulletin of the Seismological Society of America, 86(1B): S3-S18.

Hughes, A., Rood, D.H., Whittaker, A.C., Bell, R.E., Rockwell, T.K., Levy, Y., Wilcken, K.M., Corbett, L.B., Bierman, P.R., DeVecchio, D.E., Marshall, S.T., Gurrola, L.D. and Nicholson, C., 2018. Geomorphic evidence for the geometry and slip rate of a young, low-angle thrust fault: Implications for hazard assessment and fault interaction in complex tectonic environments. Earth and Planetary Science Letters, 504: 198-210.

Kew, W.S., 1924. Goelogy and oil rescources of a part of Los Angeles and Ventura Counties, California. USGS Bulletin 753.

Kilb, D., Gomberg, J. and Bodin, P., 2002. Aftershock triggering by complete Coulomb stress changes. Journal of Geophysical Research: Solid Earth, 107(B4): 2-1 - 2-14.

King, G.C., Stein, R.S. and Lin, J., 1994. Static stress changes and the triggering of earthquakes. Bulletin of the Seismological Society of America, 84(3): 935-953.

Leonard, M., 2014. Self-consistent earthquake fault-scaling relations: Update and extension to stable continental strike-slip faults. Bulletin of the Seismological Society of America, 104(6): 2953-2965.

Levi, S. and Yeats, R.S., 1993. Paleomagnetic Constraints on the Initiation of Uplift on the Santa-Susana Fault, Western Transverse Ranges, California. Tectonics, 12(3): 688-702.

Levy, Y., Rockwell, T.K., Shaw, J.H., Plesch, A., Driscoll, N.W., Perea, H., 2019. Structural modeling of the Western Transverse Ranges: An imbricated thrust ramp architecture. Lithosphere; 11 (6): 868–883. doi: https://doi.org/10.1130/L1124.1

Lin, J. and Stein, R.S., 2004. Stress triggering in thrust and subduction earthquakes and stress interaction between the southern San Andreas and nearby thrust and strike-slip faults. Journal of Geophysical Research: Solid Earth, 109(B2): 1-19.

Madden, E. H., Maerten, F., & Pollard, D. D. 2013. Mechanics of nonplanar faults at extensional steps with application to the 1992 M 7.3 Landers, California, earthquake. Journal of Geophysical Research:Solid Earth , 118 (6), 3249-3263.

Marshall, S.T., Funning, G.J., Krueger, H.E., Owen, S.E. and Loveless, J.P., 2017. Mechanical models favor a ramp geometry for the Ventura-pitas point fault, California. Geophysical Research Letters, 44(3): 1311-1319.

Marshall, S.T., Funning, G.J. and Owen, S.E., 2013. Fault slip rates and interseismic deformation in the western Transverse Ranges, California. Journal of Geophysical Research: Solid Earth, 118(8): 4511-4534.

Marshall, S.T. and Morris, A.C., 2012. Mechanics, slip behavior, and seismic potential of corrugated dip-slip faults. Journal of Geophysical Research: Solid Earth, 117(B3): 1-19.

McAuliffe, L.J., Dolan, J.F., Rhodes, E.J., Hubbard, J., Shaw, J.H. and Pratt, T.L., 2015. Paleoseismologic evidence for large-magnitude (Mw7.5–8.0) earthquakes on the Ventura blind thrust fault: Implications for multifault ruptures in the Transverse Ranges of southern California. Geosphere, 11(5): 1629-1650.

Mildon, Z.K., Roberts, G.P., Faure Walker, J.P. and Iezzi, F., 2017. Coulomb stress transfer and fault interaction over millennia on non-planar active normal faults: the Mw 6.5–5.0 seismic sequence of 2016–2017, central Italy. Geophysical Journal International, 210(2): 1206-1218.

Mildon, Z.K., Toda, S., Faure Walker, J.P. and Roberts, G.P., 2016. Evaluating models of Coulomb stress transfer: Is variable fault geometry important? Geophysical Research Letters, 43(24): 12407-12414.

Mohammadi, H., Quigley, M., Steacy, S., Duffy, B., 2019. Effects of source model variations on Coulomb stress analyses of a multi-fault intraplate earthquake sequence. Tectonophysics 766, 151–166. https://doi.org/10.1016/j.tecto.2019.06.007

Namson, J. and Davis, T., 1988. Structural transect of the western Transverse Ranges, California: Implications for lithospheric kinematics and seismic risk evaluation. Geology, 16(8): 675-679.

Nicholson, C., Kamerling, M.J., Sorlien, C.C., Hopps, T.E. and Gratier, J.-P., 2007. Subsidence, compaction, and gravity sliding: implications for 3D geometry, dynamic rupture, and seismic hazard of active basin-bounding faults in Southern California. Bulletin of the Seismological Society of America, 97(5): 1607-1620.

Nicholson, C., Plesch, A. and Shaw, J.H., 2017a. Community Fault Model Version 5.2: Updating & expanding the CFM 3D fault set and its associated fault database, 2017 SCEC Annual Meeting Proceedings & Abstracts, XXVII.

Nicholson, C., Sorlien, C., Kamerling, M.J. and Hopps, T., E, 2017b. An Integrated Onshore-Offshore Re-Evaluation of 3D Fault and Fold Geometry, Coastal Uplift and Seismic Hazard in the Santa Barbara-Ventura Area; U.S. Geological Survey Final Technical Report. Available from: https://earthquake.usgs.gov/cfusion/external_grants/reports/G16AP00100.pdf

Ogata, Y., 2005. Synchronous seismicity changes in and around the northern Japan preceding the 2003 Tokachi-oki earthquake of M8. 0. Journal of Geophysical Research: Solid Earth, 110(B8): 1-10.

Oglesby, D.D., Archuleta, R.J. and Nielsen, S.B., 1998. Earthquakes on dipping faults: the effects of broken symmetry. Science, 280(5366): 1055-1059.

Oglesby, D.D. and Day, S.M., 2001. Fault geometry and the dynamics of the 1999 Chi-Chi (Taiwan) earthquake. Bulletin of the Seismological Society of America, 91(5): 1099-1111.

Olson, E.L. and Cooke, M.L., 2005. Application of three fault growth criteria to the Puente Hills thrust system, Los Angeles, California, USA. Journal of Structural Geology, 27(10): 1765-1777.

Pace, B., Bocchini, G.M. and Boncio, P., 2014. Do static stress changes of a moderate-magnitude earthquake significantly modify the regional seismic hazard? Hints from the L'Aquila 2009 normal-faulting earthquake (Mw 6.3, central Italy). Terra Nova, 26(6): 430-439.

Parsons, T., Stein, R.S., Simpson, R.W. and Reasenberg, P.A., 1999. Stress sensitivity of fault seismicity: A comparison between limited-offset oblique and major strike-slip faults. Journal of Geophysical Research: Solid Earth, 104(B9): 20183-20202.

Pei, Y., Paton, D.A., Knipe, R.J., Lickorish, W.H., Li, A. and Wu, K., 2018. Unraveling the influence of throw and stratigraphy in controlling subseismic fault architecture of fold-thrust belts: An example from the Qaidam Basin, northeast Tibetan Plateau. AAPG Bulletin, 102(6): 1091-1117.

Plesch, A., Shaw, J.H., Benson, C., Bryant, W.A., Carena, S., Cooke, M., Dolan, J., Fuis, G., Gath, E. and Grant, L., 2007. Community fault model (CFM) for southern California. Bulletin of the Seismological Society of America, 97(6): 1793-1802.

Quigley, M.C., Jiménez, A., Duffy, B., King, T.R., 2019. Physical and Statistical Behavior of Multifault Earthquakes: Darfield Earthquake Case Study, New Zealand. J. Geophys. Res. Solid Earth 124, 4788–4810. https://doi.org/10.1029/2019JB017508

Rice, J.R., 1992. Fault stress states, pore pressure distributions, and the weakness of the San Andreas fault, International geophysics. Elsevier, pp. 475-503.

Rockwell, T., 1983. Soil chronology, geology, and neotectonics of the northcentral Ventura basin. PhD Thesis, University of California: Santa Barbara, Santa Barbara.

Rockwell, T., 1988. Neotectonics of the San-Cayetano Fault, Transverse Ranges, California. Geological Society of America Bulletin, 100(4): 500-513.

Rockwell, T.K., Clark, K., Gamble, L., Oskin, M.E., Haaker, E.C. and Kennedy, G.L., 2016. Large Transverse Range Earthquakes Cause Coastal Upheaval near Ventura, Southern California. Bulletin of the Seismological Society of America, 106(6): 2706-2720.

Ryan, K.J., Geist, E.L., Barall, M. and Oglesby, D.D., 2015. Dynamic models of an earthquake and tsunami offshore Ventura, California. Geophysical Research Letters, 42(16): 6599-6606.

Rydelek, P.A. and Sacks, I.S., 1999. Large earthquake occurrence affected by small stress changes. Bulletin of the Seismological Society of America, 89(3): 822-828.

Schlueter, J.C., 1976. Geology of the Upper Ojai-Timber Canyon Area Ventura County, California, Ohio University, Ohio.

Scholz, C.H., 1990. The mechanics of earthquakes and faulting. Cambridge university press.

Sorlien, C.C., Gratier, J.-P., Luyendyk, B.P., Hornafius, J.S. and Hopps, T.E., 2000. Map restoration of folded and faulted late Cenozoic strata across the Oak Ridge fault, onshore and offshore Ventura basin, California. Geological Society of America Bulletin, 112(7): 1080-1090.

Sorlien, C.C. and Nicholson, C., 2015. Post-1 Ma Deformation History of the Pitas Point-North Channel-Red Mountain Fault System and Associated Folds in Santa Barbara Channel, California. Grant report from award number: G14AP00012. Available from: https://earthquake.usgs.gov/cfusion/external_grants/reports/G14AP00012.pdf

Stahl, T., Quigley, M.C., McGill, A., Bebbington, M.S., 2016. Modeling earthquake moment magnitudes on imbricate reverse faults from paleoseismic data: Fox peak and forest creek faults,

South Island, New Zealand. Bull. Seismol. Soc. Am. 106, 2345–2363. https://doi.org/10.1785/0120150215

Tan, S., Clahan, K. and Irvine, P., 2004. Geologic map of the Santa Paula 7.5-minute quadrangle, Ventura County, California, 1: 24, 000. California Geological Survey, California.

Toda, S., Stein, R.S., Reasenberg, P.A., Dieterich, J.H. and Yoshida, A., 1998. Stress transferred by the 1995 Mw= 6.9 Kobe, Japan, shock: Effect on aftershocks and future earthquake probabilities. Journal of Geophysical Research: Solid Earth, 103(B10): 24543-24565.

Toda, S., Stein, R.S., Richards-Dinger, K. and Bozkurt, S.B., 2005. Forecasting the evolution of seismicity in southern California: Animations built on earthquake stress transfer. Journal of Geophysical Research: Solid Earth, 110(B5): 1-17.

Verdecchia, A. and Carena, S., 2016. Coulomb stress evolution in a diffuse plate boundary: 1400 years of earthquakes in eastern California and western Nevada, USA. Tectonics, 35(8): 1793-1811.

Weber, F., Kiessling, E., Sprotte, E., Johnson, J., Sherburne, R. and Cleveland, G., 1976. Seismic hazards study of Ventura County. California: California Department of Conservation, California Division of Mines and Geology Open-File Report: 76-5.

Wedmore, L., Walker, J.F., Roberts, G.P., Sammonds, P., McCaffrey, K. and Cowie, P., 2017. A 667 year record of coseismic and interseismic Coulomb stress changes in central Italy reveals the role of fault interaction in controlling irregular earthquake recurrence intervals. Journal of Geophysical Research: Solid Earth, 122(7): 5691-5711.

Winterer, E.L. and Durham, D.L., 1962. Geology of southeastern Ventura Basin, Los Angeles County, California. 2330-7102.

Wright, T.L., 1991. Structural geology and tectonic evolution of the Los Angeles basin, California. Active Margin Basins, 52: 35-134.

Yeats, R.S., Huftile, G.J. and Grigsby, F.B., 1988. Oak-Ridge Fault, Ventura Fold Belt, and the Sisar Decollement, Ventura Basin, California. Geology, 16(12): 1112-1116.

Yeats, R.S., Huftile, G.J. and Stitt, L.T., 1994. Late Cenozoic tectonics of the east Ventura basin, Transverse Ranges, California. AAPG bulletin, 78(7): 1040-1074.

Yerkes, R., Sarna-Wojcicki, A. and Lajoie, K., 1987. Geology and Quaternary deformation of the Ventura area. Recent reverse faulting in the Transverse Ranges, California. US Geological Survey Professional Paper, 1139: 169-178.

Ziv, A. and Rubin, A.M., 2000. Static stress transfer and earthquake triggering: No lower threshold in sight? Journal of Geophysical Research: Solid Earth, 105(B6): 13631-13642.

Table 1. Summary of well data for wells with 'high' confidence

Well Name	Well No [a]	API	Latitude (°)[b]	Longitude (°)[b]	Possible Fault Evidence	Fault Depth (m[c])	Data Source	Cross Section [d]
Pagenkopp 1	1	11106059	34.43843	-118.949713	*~120 m of Pico Formation interpreted within Saugus Formation in resistivity log from 1000-1120 m*	1120	Hopps et al. (1992)	A-A'
Santa Paula Unit 1	2	11106064	34.448828	-118.955882	*Zone of highly disturbed dips in dipmeter data from 1000–1500 m, increase in dip from 15°–50° between ~1350–1850 m. Change in R and SP at 1650 m*	1650	Hopps et al. (1992)	A-A'
Lagomarsino-Butler 1	3	11106073	34.399361	-119.038245	*Abrupt change in dip from 45°S to 30°N at 480 m and from 50°N to 40°S at 1055 m. Lower change in dip corresponds to disturbances in R & SP.*	1055	Hopps et al. (1992)	B-B'
Rudolph 22-25	4	11120986	34.405526	-119.039616	*Abrupt change in dipmeter from 60°N to 50°S at 810 m. Increase in dip from 45°S to 75°S between 900 m and 1375 m.*	~1300	Hopps et al. (1992)	B-B'
Sharp et al 1	5	11106076	34.384737	-119.062215	*Zone of highly disturbed dips in dipmeter data and highly variable R & SP from surface to 500 m. Abrupt decrease in dip from 60°N to 20°S at 280 m and 40°S to flat at 500 m.*	280	Hopps et al. (1992)	C-C'
Signal-Powell 1	6	11106078	34.387442	-119.0688	*Abrupt decrease in dip from 60°S to 20°S at 250m and an increase in dip from 20°S to 45°S at 550 m which corresponds to a spike in SP.*	550	Hopps et al. (1992)	C-C'
Ojai 67	8	11101069	34.426699	-119.105686	*Band of Miocene fossils sandwiched between Pliocene fossils correlating to change in R at 1800 m.*	1800	This study, Huftile (1988)	C-C'
Hamp B69	13	11121275	34.434858	-119.095644	*Abrupt decrease in dipmeter reading from 65°N to 17°N at 1990 m.*	1990	Huftile (1988)	n/a
Arco 6	14	11120471	34.43033	-119.09972	*Decrease in dipmeter readings from 85°N to 45°N at 2050 m*	2050	Hopps et al. (1992)	C-C'

a: Well No refers to location on map in Figure 1b and is also noted in Figures 2, 3, & 4 (if applicable)
b: Latitude and longitude refer to the surface location of the well. The actual location of the fault evidence may be away from this location if the well has significant deviation from vertical
c: Fault depth in meters below sea level
d: See Figure 3 for cross sections
R = Resistivity, SP = Spontaneous potential

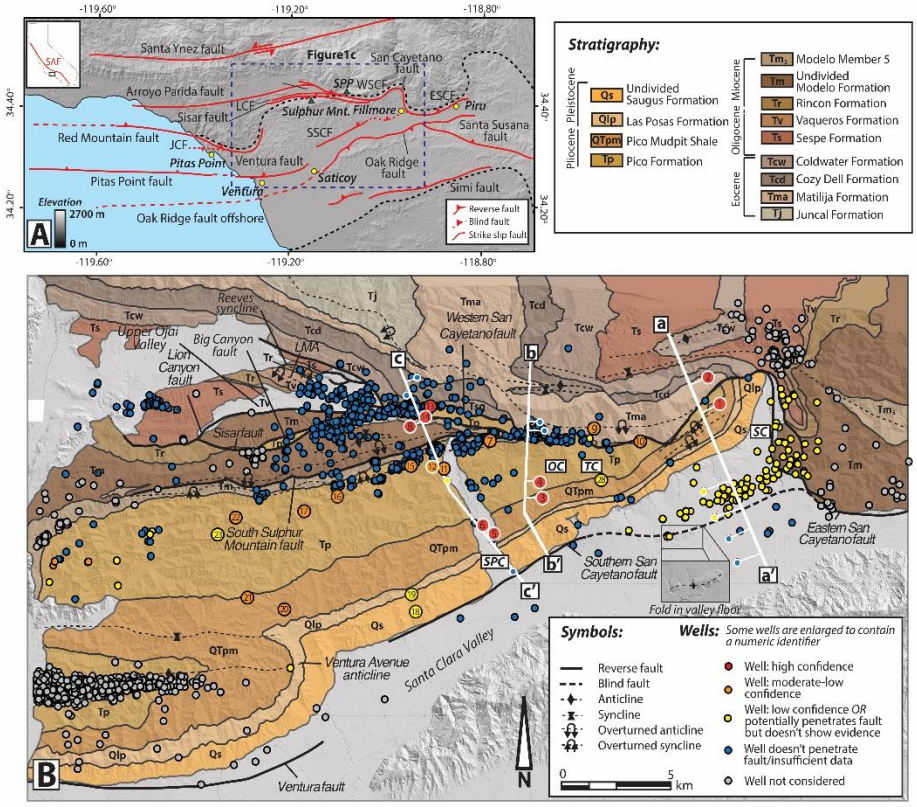

Figure 1. Major structures and geological units in the Ventura basin. A) Fault map of the study area. Yellow circles are the location of towns and green triangles are mountain peaks referred to in the text. The outline of the Ventura basin is denoted with the dashed black line. The blue dashed box shows the limits of B and the figure is located in UTM zone 11N. B) Geological map of the study area showing major Cenozoic sedimentary units and the locations of petroleum wells discussed in the text. Geologic units are based on the Dibblee Foundation maps (see section 3 for references) with the nomenclature of Campbell et al. (2014). Wells are color coded based on the degree to which the potential fault cuts in well data provide evidence for the low-angle Southern San Cayetano fault. Key wells are enlarged relative to other wells to include the numeric identifiers for the wells in Tables 1 and S1, and Figures 2, 3, and 4. The lines in white represent the cross sections included in Figure 3 and well projections on to the section line are represented with thin white lines. Well locations are from California Department of Conservation online well database. SPP = Santa Paula Peak, SSCF = Southern San Cayetano fault, LMA = Lion Mountain anticline, JCF = Javon Canyon fault, LCF = Lion Canyon fault, WSCF = Western San Cayetano fault, ESCF = Eastern San Cayetano fault, SAF = San Andreas Fault, TC = Timber Canyon, OC = Orcutt Canyon, SPC = Santa Paula Creek.

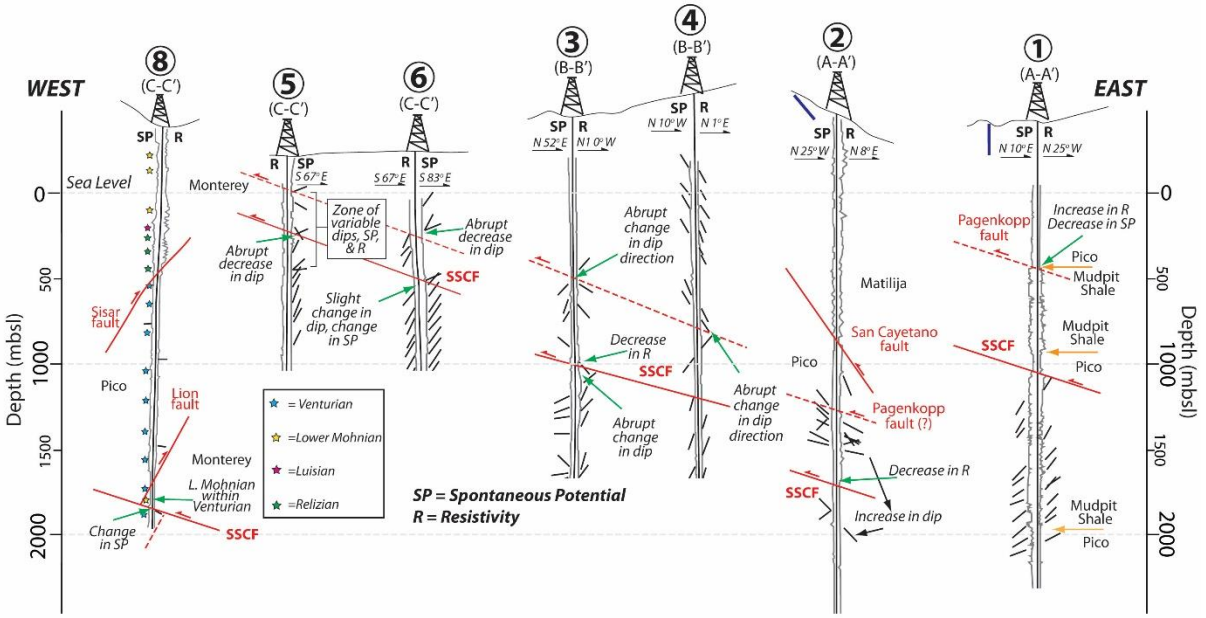

Figure 2. Summary of data from key wells that we interpret to provide evidence the low-angle Southern San Cayetano fault (SSCF). Blue lines are surface bedrock dips from published geological maps (see text for references). Dipmeter data (black ticks next to wells) are taken from Hopps et al. (1992). The number above the wells refers to the number assigned to the wells in Table 1, which contains full details of all wells. The letters below the well number refer to the cross sections in Figure 3. Well locations are shown in Figure 1. SP = Spontaneous potential, R = Resistivity, mbsl = meters below sea-level.

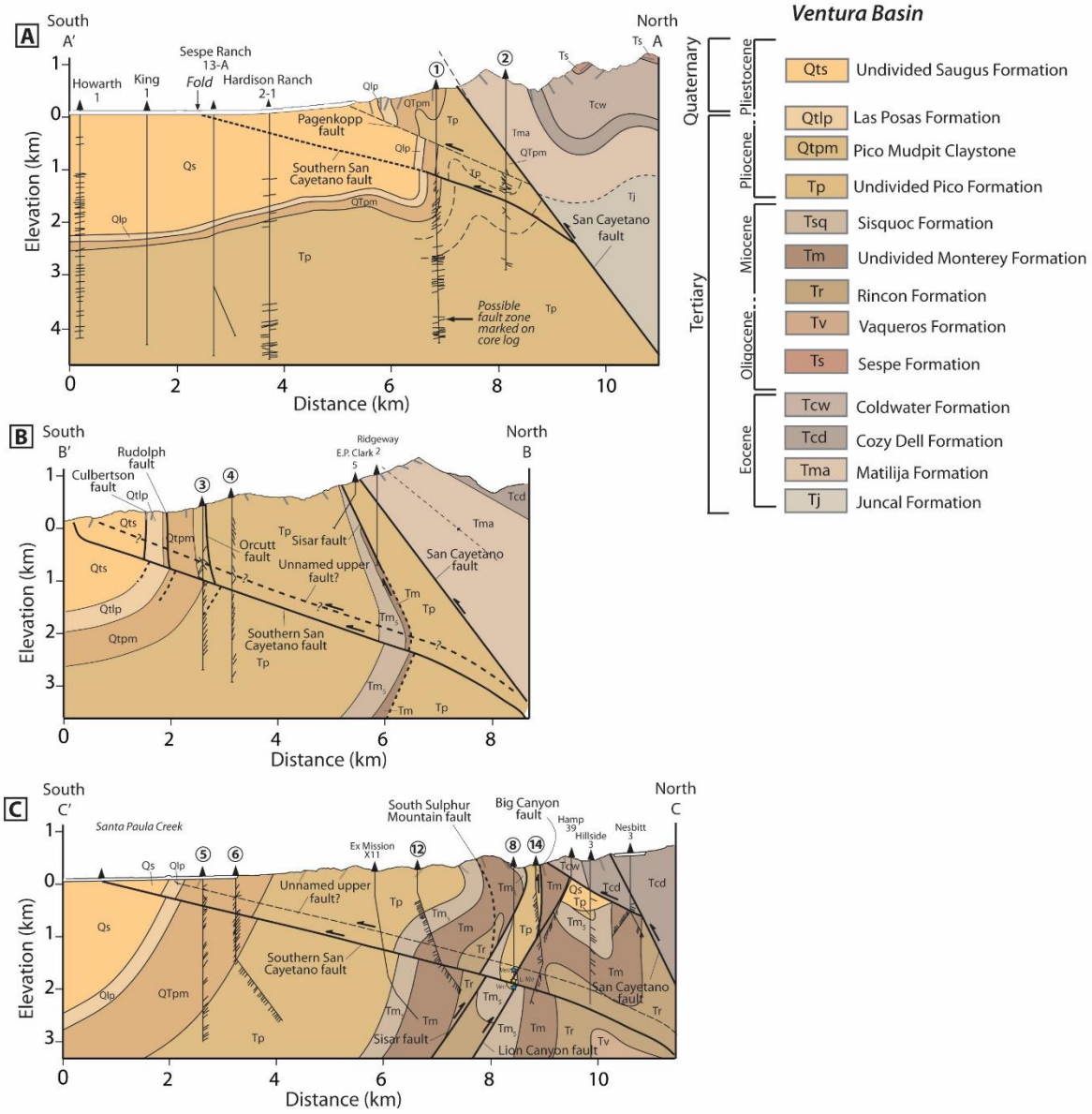

Figure 3. Cross sections through the low-angle Southern San Cayetano fault (SSCF). Fault offset of ~110 m for the SSCF is based on an inferred age for the SSCF of ~58 ka and a maximum slip rate of 1.9 mm yr^{-1} (Hughes et al., 2018) and is not based on evidence from well data. A) Section A-A' is a geological section through the eastern end of the low-angle SSCF. B) Section B-B' is a geological section through the center of the low-angle SSCF adapted from Hughes et al. (2018). C) Section C-C' is a geological section towards the western end of the low-angle SSCF. Well data are extracted from Hopps et al. (1992) and structure for all faults and geological units apart from the SSCF is adapted from Hopps et al. (1992) using the nomenclature of Campbell et al. (2014). Surface dips (grey ticks) are from published geological maps (see text for references). Geometry of the SSCF is based on data described in section 4.1. Full well details and description of fault evidence are included in Table 1 and further details on wells is presented in Table S1.

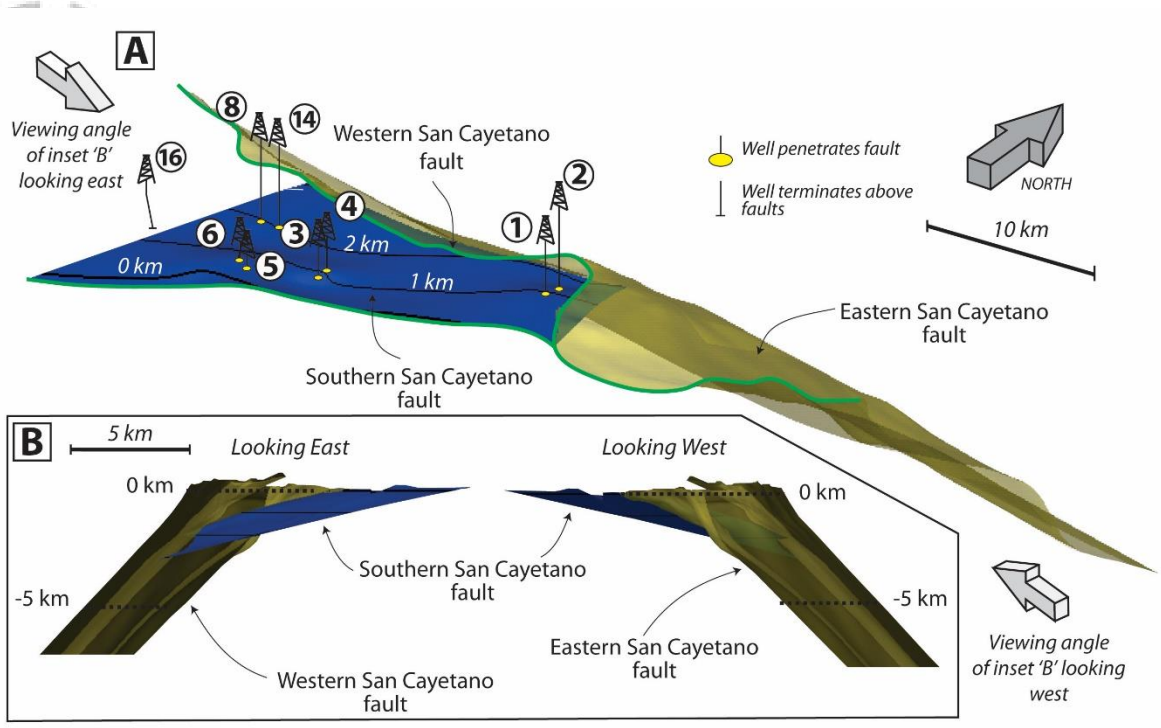

Figure 4. Three-dimensional fault model for the low-angle Southern San Cayetano Fault (SSCF). A) Oblique three-dimensional view of the SSCF (blue) looking northwest and down-dip of the San Cayetano fault (yellow). The well numbers refer to wells described in Table 1 and S1, and the green lines are fault surface traces. B) Cross sections looking east and west to demonstrate the connection of the low-angle SSCF with the San Cayetano fault in the subsurface.

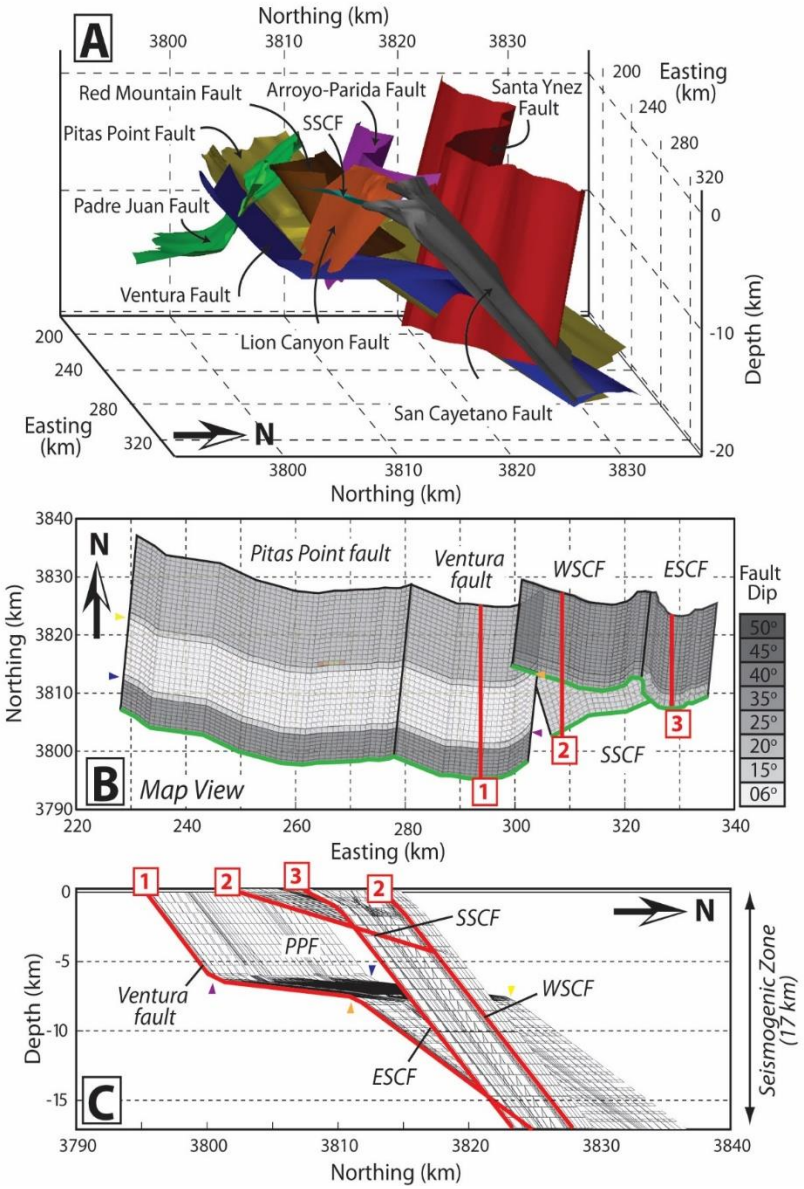

Figure 5. Set up for static Coulomb stress models. A) Three-dimensional model of faults in the Ventura basin looking west. Fault surfaces are taken from the Southern California Earthquake Center three-dimensional Community Fault Model (Plesch et al., 2007; Nicholson et al., 2017a). B) Map view showing the extent of faults included in the static Coulomb stress models. The green lines are fault surface traces and the red lines are lines of the cross sections in C with numbers corresponding to the relevant section. The fault surfaces are color coded by fault dip and the fault mesh is outlined by the small rectangles. Colored triangles show corresponding points in B and C. C) View looking west showing the geometry of the fault surfaces used in the stress modeling in cross section (red lines). The fault mesh is outlined with the black rectangles. PPF = Pitas Point fault, ESCF = eastern section of the San Cayetano fault, WSCF = western section of the San Cayetano fault, SSCF = low-angle Southern San Cayetano fault.

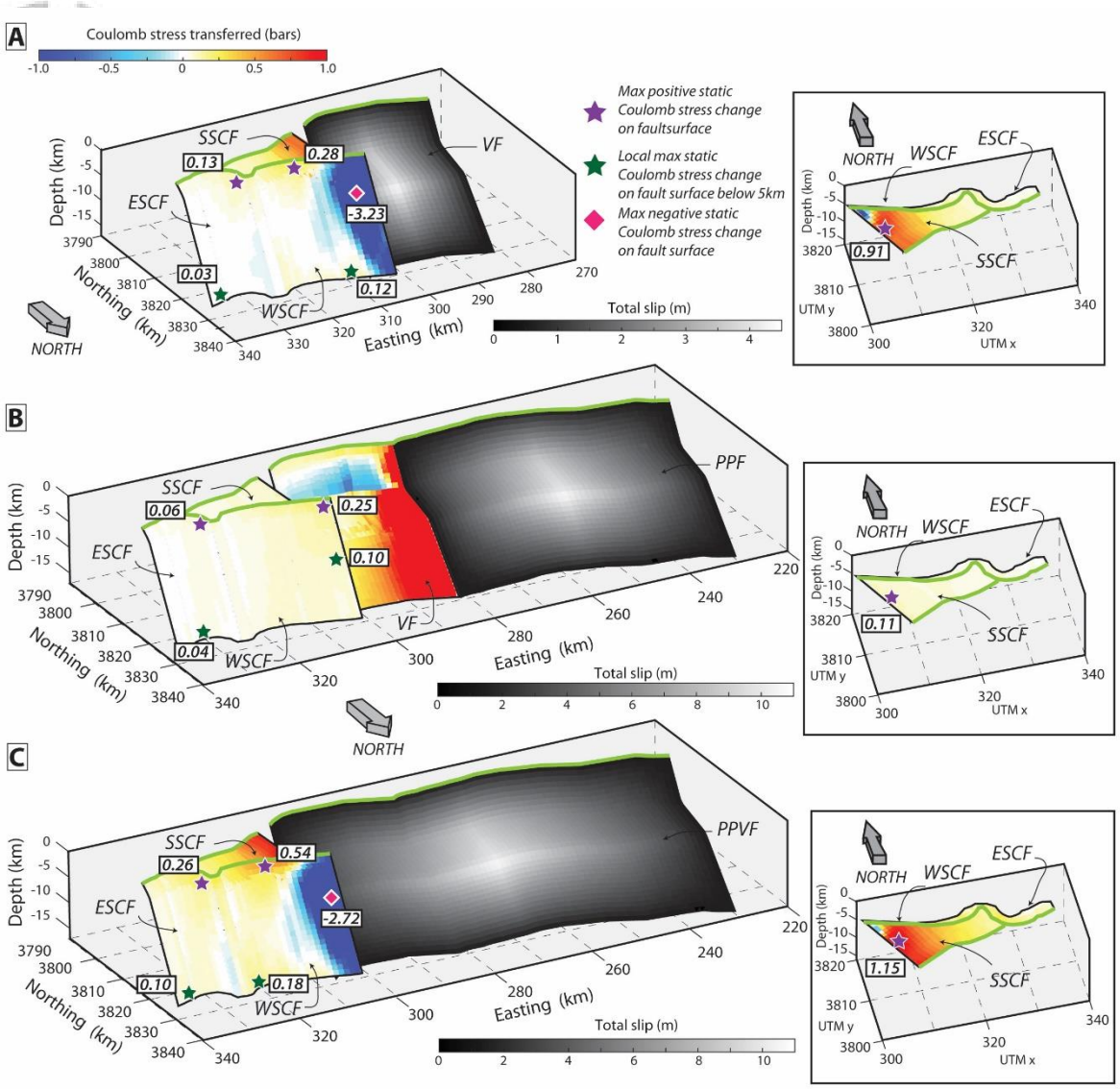

Figure 6. Modeled static Coulomb stress change ($\Delta\sigma_f$) for pure dip-slip ruptures imparted on the San Cayetano fault looking obliquely southwest. The inset is looking northeast and down-dip of the San Cayetano fault to show the results on the low-angle Southern San Cayetano fault (SSCF). Other proximal faults such as the Red Mountain, Sisar, Lion Canyon, Padre Juan, and Arroyo-Parida faults are not included in the models to simplify the figure and to highlight $\Delta\sigma_f$ on the San Cayetano fault. A) Rupture simulated on the Ventura fault (VF). B) Rupture simulated on the Pitas Point fault (PPF). C) Rupture simulated on the entire Pitas Point/Ventura fault (PPVF). Stress change is set to +/- 1 bar to highlight the patterns of modeled stress change below this value. The green lines are fault surface traces. The green stars represent maximum positive $\Delta\sigma_f$ below a depth of 5 km, because most large earthquakes are generally thought to nucleate below this depth. The numbers in the white boxes are the magnitude of $\Delta\sigma_f$ in bars. ESCF = eastern section of the San Cayetano fault (ESCF), WSCF = western section of the San Cayetano fault.

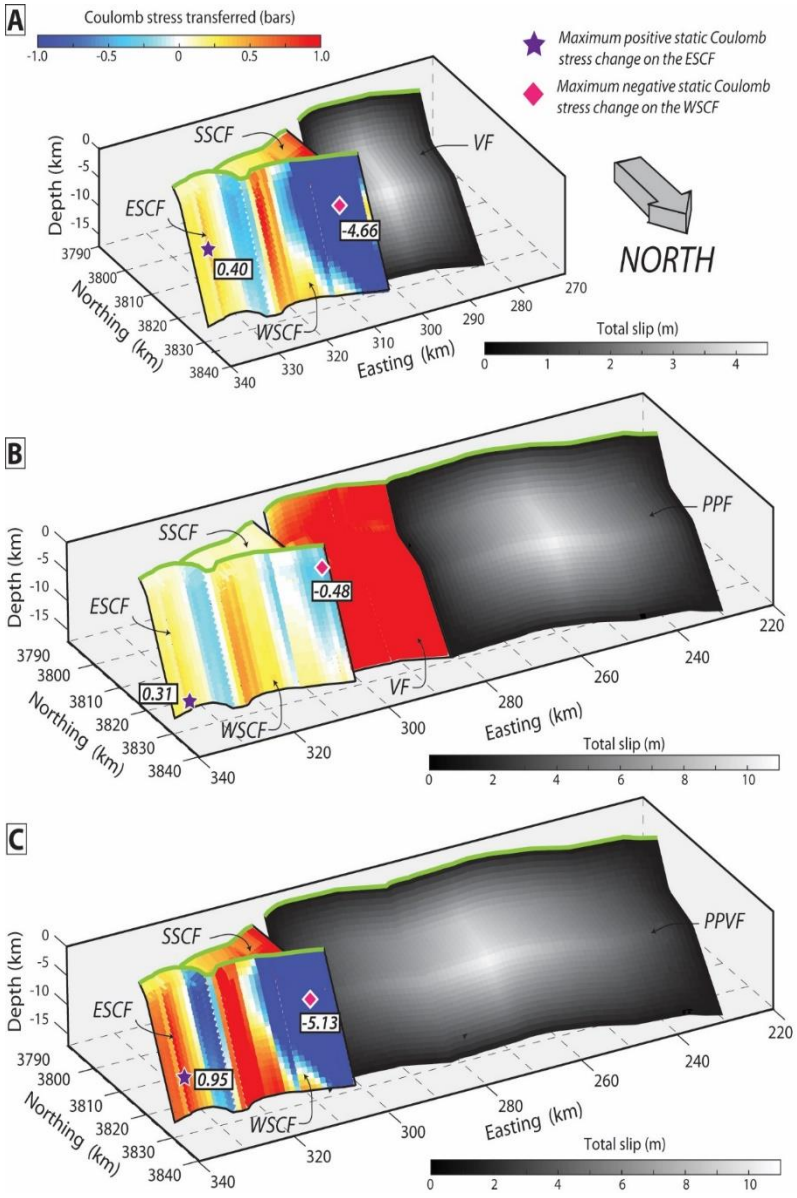

Figure 7. Modeled static Coulomb stress change ($\Delta\sigma_f$) imparted on the San Cayetano fault for oblique left-lateral ruptures. The view is looking obliquely southwest. A) Rupture simulated on the Ventura fault (VF). B) Rupture simulated on the Pitas Point fault (PPF). C) Rupture simulated on the combined Pitas Point/Ventura fault (PPVF). Stress change is set to +/- 1 bar to facilitate a comparison with the results for pure dip-slip ruptures in Figure 6. The green lines are fault surface traces. The numbers in the white boxes are the magnitude of $\Delta\sigma_f$ in bars. ESCF = eastern section of the San Cayetano fault (ESCF), WSCF = western section of the San Cayetano fault.

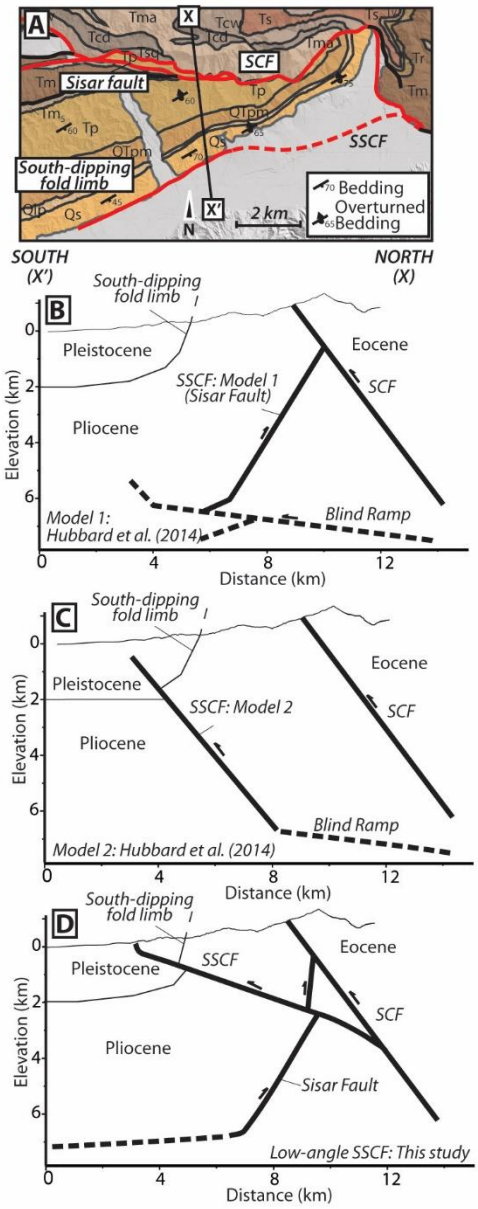

Figure 8. Schematic representations of the various models for the Southern San Cayetano fault (SSCF). A) Geologic map showing the south-dipping fold limb in the footwall of the San Cayetano fault. Faults included in B, C, and. D are solid red lines. Bedding readings are taken from Dibblee Foundation maps (see text for references). The line X–X' is the approximate line of the schematic cross sections. Key to stratigraphic labels is included in Figure 1. B) Schematic representation of the south-dipping model 1 of Hubbard et al. (2014). C) Schematic representation of the north-dipping model 2 of Hubbard et al. (2014). D) Schematic representation of the low-angle SSCF based on data presented in this study.